Univerzita Karlova v Praze
Matematicko-fyzikální fakulta

DIPLOMOVÁ PRÁCE

Petr Chaloupka

Multibosonové jevy na RHIC

Ústav částicové a jaderné fyziky
Vedoucí diplomové práce: prom. fyz. Michal Šumbera CSc.

Studijní program: Fyzika, Jaderná a subjaderná fyzika

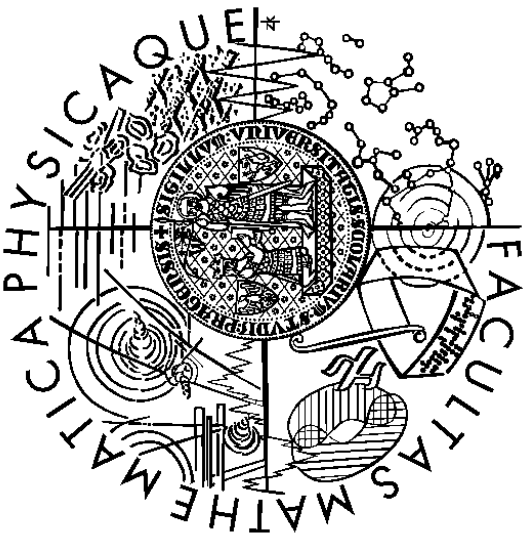

Prohlašuji, že jsem svou diplomovou práci napsal samostatně a výhradně s použitím citovaných pramenů. Souhlasím se zapůjčováním práce.

V Praze dne 19.4.2002 Petr Chaloupka

Multiboson effects at RHIC

Petr Chaloupka

Contents

Chapter 1

Introduction

In June 2000 the Relativistic Heavy Ion Collider (RHIC)[1] at the Brookhaven National Laboratory (BNL) started to collide two beams of gold ions at the total energy of 130 GeV per nucleon pair in the center of mass system[2]. In the year 2001 RHIC achieved it's maximum proposed energy of $\sqrt{S_{NN}} = 200\,GeV$ which corresponds to 20 TeV beam in fixed target experiments. The experiments at RHIC[3] continue in the ultra-relativistic heavy-ion research that was previously carried out at the Alternating Gradient Synchrotron (AGS)[4] in BNL and Super Proton Synchrotron (SPS) in CERN[5]. The RHIC makes possible to extend this research to energy levels that were never before achieved at Earth.

The primary physics goal of the experiment is to collide heavy nuclei in order to study properties of strongly interacting nuclear matter under extreme temperatures and densities. These laboratory conditions correspond to conditions in the very early universe. With the energies of RHIC it's possible to recreate and study the matter as it existed couple microseconds after the Big Bang. As the theory of quantum chromodynamics (QCD) predicts, the hadronic matter under such conditions should undergo a phase transition and create a completely new form of matter with extraordinary physical properties. This matter is analogous to the plasma phase of an ordinary atomic matter and is thus called quark gluon plasma (QGP). In such a QGP quarks and gluons are no longer confined in hadrons by the strong force, but are "released" into a larger region,where they can propagate as free particles. These particles are not, in contrast to normal matter, color-less.

The confirmation of existence of QGP is not a case of measuring one or two well defined observable variables, but rather quite a large number of

different signals. The occurrence of the predicted phase transition should manifest itself in simultaneous changes in these signals.

The purpose of this work is to study effects connected with high multiplicity production of bosons in the gold-gold collisions. The data for this work were measured during a year 2001 by the Solenoidal Tracker at RHIC (STAR) experiment[22] at the energy of $\sqrt{S_{NN}} = 130\ GeV$. The aim is to study multiparticle correlations in the region of small transversal momentum that is mainly populated by pions. This part of the momentum spectrum allows to study effects possibly coming from the nonperturbative (thermal) part of the QGP to hadronic matter transition. We use the apparatus of *normalized factorial moments*[6] to extract the information about multiparticle correlations in small pseudorapidity windows.

The area of small transversal momentum spectrum should be accessible by a newly installed Silicon Vertex Tracker(SVT)[23, 24]. This is a large area multidetector system of *silicon drift detectors*; quite a new type of a silicon detector with very interesting capabilities, that has previously been used only in few experiments. Part of this work deals with a drift speed calibration of this detector, exploring the possibility of using implanted injectors of electric charge.

Chapter 2

Physics at RHIC: From QCD to QGP

2.1 Basic properties of QCD

It is generally held that the physics of the strong interaction is well described by the theory of *Quantum chromodynamics* (QCD)[7][8]. This theory is based on the same frame of quantum field theories[9] that are also used for the theory of *quantum electrodynamics* (QCD) and the weak interaction. It is supposed that the QCD belongs to the class of field theories known as the *gauge filed theories* [10]. It means that the properties of the interactions of the fields can be deduced from a special invariance requirement of the Lagrangian. This invariance is called *local gauge invariance*. The quanta of the QCD field are the *quarks* and quanta of the gauge field are the *gluons*. If the gluons were to have a non-zero rest mass in such a theory, then the Lagrangian containing them would not be locally gauge invariant. In order to maintain the theory locally gauge invariant the gluons must be massless like the *photons* - the gauge field quanta of the electromagnetic interaction.

The interaction between quarks and antiquarks depends on the color of the interacting particles. The color is an intrinsic quantum number carried by quarks and gluons. There are three possible colors quarks can have: (R)ed, (G)reen, (B)lue. A quark with a color can interact with another quark via exchange of a gluon. There are eight gluons belonging to the $SU(3)$ color group.

In the phenomenological quark model[7], baryons are described as three-

quark bound states, and mesons as the quark-antiquark bound states. There is no evidence, so far, that there exists any particle not belonging to the color singlet. Thus all the observed particles in the nature seem to be colorless. There also has never been observed a single quark. On the other hand, deep-inelastic experiments has shown that with a large momentum transfer the quarks inside the hadrons behave as if they were free particles. This all suggests that the strong interaction is very strong on large distances, but rather weak on very short distances.

QCD differs from QED mainly by being *non-Abelian*. In non-Abelian gauge filed theory the gauge filed operators do not commute. The most important effect of this is that the gluons carry color charge, unlike the photons which do not have an electric charge. It implies that the gluons can interact with each other, contrary to the photons in QED. This self-interaction of gluons is the reason of the *confinement* of the quarks inside the hadrons. The relative strength of the interaction in QCD can be described by coupling constant which depends on the momentum transfer q involved in the interaction. The so called *running constant* $\alpha_s(q)$ is:

$$\alpha_s(q) = \frac{12\pi}{(32 - 2N_f) \ln \frac{q^2}{\Lambda^2_{QCD}}} , \tag{2.1}$$

where N_f is number of quark flavors taken under consideration, and Λ_{QCD} is the fundamental measure of the QCD coupling. Λ_{QCD} is experimentally determined to be $\approx 200MeV$.

When the momentum transfer is large, the coupling constant $\alpha_S(q)$ is small. On the other hand, if the distance scale is large, the interaction is strong. The decrease of the strength of the strong interaction at small distances is called the *asymptotic freedom*[31]. This behavior of coupling constant crates two different domains of QCD calculation. In the domain of small coupling constant the means of *perturbative* calculations can be implemented. These processes are thus fully calculable. In the domain of strong coupling the perturbative treatment will fail. It is then necessary to use other non-perturbative techniques, like, for example, the QCD lattice computations[11].

2.2 Transition to quark-gluon plasma

The lattice QCD calculations predict, at sufficiently high temperatures, an entirely new form of matter. This matter is analogous to the plasma phase of ordinary atomic matter and is therefore called the *quark-gluon plasma* (QGP). In the ordinary atomic matter, whose behavior is governed mainly by quantum electrodynamics, at high temperatures and densities, the single atoms start to loose their individual identities and the matter becomes a mixture of individual free electrons and nuclei. In the QGP the quarks and gluons are also no longer confined inside of hadrons, but can propagate throughout the whole medium. Even though the whole medium has an overall zero color charge, the quarks behave as single free particles carrying the color charge.

The theoretical QCD study at lattice allowed to estimate the critical temperature needed for such a phase transition from the hadronic matter to the supposed QGP phase as $150 \sim 200 MeV$. Because in the beginning of our universe, according to the *Big Bang* model, existed such high temperatures in the very dense matter, is commonly believed that the QGP existed for some time. Today a QGP is expected to exist in the very dense matter inside of neutron stars.

2.3 The ultrarelativistic heavy ion collision

The major goal of nowadays high energy heavy ion physics is to create condition under such the QGP state of matter could be created and studied in the laboratory. The use of heavy ions has an advantage over the use of lighter particles or ions in creating larger interaction volumes. The larger interaction volume with higher number of participating particles allows the use of macroscopic variables and better environment for the use of statistics. The system can then be better described in terms of fewer fundamental variables, which simplifies the whole problem. The larger volume allows the partons of the collided nuclei to scatter and rescatter several times, thus depositing more energy in the interaction volume. If the system is large, compared to the mean free paths of the particles inside, the particles scatter on their way out and cannot easily escape. The objective is to achieve a long living and big enough system in which the thermal equilibrium could be reached or at least approached with enough high temperatures and densities to produce

the quark-gluon plasma.

In heavy-ion collisions the geometry of the collision plays an important role because of the relatively "big" sizes of the nuclei. The geometry of the collision can be defined in the terms of the participant-spectator model, as shown in the Figure 2.1.

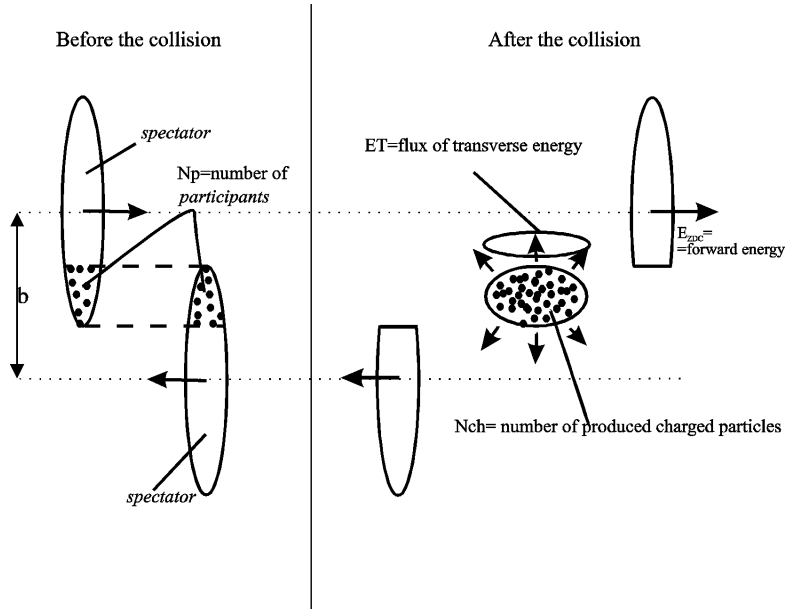

Figure 2.1: Schematic view of the ultrarelativistic heavy-ion collision in the CMS frame.The nuclei are pancake-shaped because of the extreme relativistic Lorenz contraction.

Nucleons taking part in the primary collision are called *participants* and the non interacting nucleons are called *spectators*. The *centrality* is characterized by the impact parameter b.

It is important to distinguish between different centralities since the amount of deposited energy in the collision region depends on the geometry of the collision. The more central is the collision, the larger amount of energy is deposited. The impact parameter b and the number of participants N_p are not directly observable variables and have to be therefore deduced from other measured variables using suitable model (the Glauber model of nucleus-nucleus collisions[12]). The measured quantities, from which the centrality can be deduced, are usually the energy carried away by the specta-

tors E_{ZDC} (measured by the zero degree calorimeter), number of produced charged particles N_{ch} and the transversal energy $E_{\perp}$.

As the nuclei collide, the participating baryons loose energy and slow down. There are two opposing extreme pictures. In the first picture the participating baryons are fully stopped in the reaction zone where the energy was deposited. In the case of *full stopping* the collision should produce a quark-gluon plasma with high baryon content. The opposite, most often considered, case is the so called *full transparency* regime. In this regime, at very high energies (about $100\,GeV$ per nucleon pair in CMS), the participants after collision have still enough momentum to proceed out of the collision region. As the consequence, a large amount of energy is deposited in a small region with very small net baryon charge. This can be of special interest from the point of view of astrophysics since the net baryon content of the early universe was small.

The space-time evolution of the heavy-ion collision is schematically described in Figure 2.2. The $z - axis$ represents the beam direction and the collision occurs at time $t = 0$ at $z = 0$. The evolution after the collision can be divided into couple different stages that are connected with different measurable signals. The first stage is immediately after the collision and is characterized by the formation of high density energy region. After a short time of the order of $\tau_0 = 1 fm/c$ partons materialize and their rescattering leads to the thermalization of the system. In the third phase the hot ball of quark-gluon plasma expands rapidly and cools down till it reaches the critical temperature at time τ_h at which the hadrons start to form. In the fourth phase the hadrons are created from the plasma while the whole system keeps expanding and cooling down. This is the *mixed phase*. This continues to the point of *chemical freeze-out* at time τ_{cf} when the hadrons cease to exchange the quarks and the hadron gas is formed. Then, the still interacting, system of hadrons expands further to the point of the *thermodynamical freeze-out* at time τ_f when hadrons stop rescattering and are emitted.

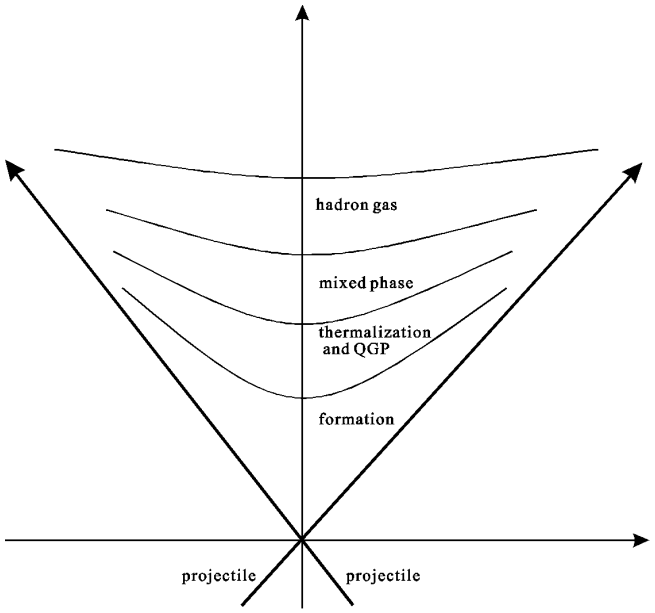

Figure 2.2: Space-time evolution of the nucleus-nucleus collision.

Chapter 3

The phase transition to QGP

3.1 The bag model of hadrons

The theoretical results from the lattice gauge theory show that, when the distance between quarks is comparable to the sizes of hadrons, the quarks interact with an effective interaction which grows approximately linearly with the their distance. This means that large scale behavior of quarks is characterized by their confinement in hadrons. This can be intuitively visualized by the following Figure 3.1.

As the distance between quark and antiquark grows, the strength and and potential energy grows as well. This continues to the moment till it's energetically more favorable to produce another quark-antiquark pair along the path. The newly produced quark is then bound with the antiquark, and the newly produced antiquark is bound to the quark, creating two new color-less hadrons with the quarks confined inside of them.

Event thought the perturbative QCD cannot describe the behavior of the confined quarks, there are some phenomenological models that can give some relevant description. One approach is the *bag model*[14], where the confining forces resulting from the nonpertubative QCD are replaced by a vacuum pressure outside of the hadron. In this, more precisely called *MIT bag model*, quarks are treated as massless particles inside a bag of a finite dimension, and are infinitely massive outside of the bag. Confinement of the quarks is then the result of the balance between the inward pressure of the bag and the outward pressure arising from non-zero kinetic energy of the quarks inside. In this model the bag pressure B is a phenomenological

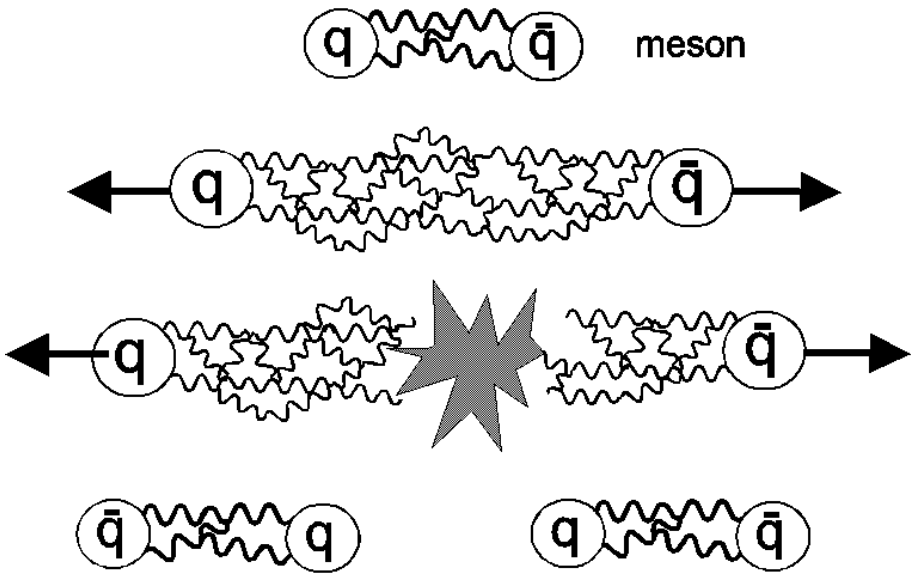

Figure 3.1: Intuitive view of the quark confinement.

constant that substitutes the nonperturbative effects of QCD.

In [12] is shown that an estimate of the bag pressure can be obtained by considering massless fermions inside of a sphere of radius R. Using the Dirac equation for massless fermions $\gamma \cdot \mathbf{p}\psi = 0$ and the requirement of the confinement, which is the same as to require that the scalar fermion density $\psi\overline{\psi}$ vanishes at the distance of R. From this we get the expression 3.1 for the relation between the bag pressure B and the radius R

$$B = \left(\frac{2.04N}{4\pi}\right)\frac{1}{R^4}, \tag{3.1}$$

where N is the number of the quarks in the bag. Taking the measured value of $R = 0.8fm$ for 3 quark system, we obtain the estimate of the value of the bag pressure $B^{1/4} = 206MeV$.

This description allows a simple explanation of the phase transition form the normal hadronic matter, with the quarks confined in the hadrons, to the deconfined phase. It can be seen that if, in this model, the pressure exerted from the quarks inside rises, there will be a point when the pressure from inside exceeds the pressure of the bag. At this point the bag pressure will not be able anymore to hold the quarks inside of the hadron. The quarks

and gluons will then undergo a phase transition from the confined to the *deconfined state*.

Main condition for the phase transition is then the big rise of the pressure from the quarks inside the bag. There are two different conditions under which the pressure from the quarks can be increased:

1. high temperature of the matter
2. very high baryon density

Any of these conditions by itself, or their combination, should be sufficient to create the deconfined phase of the quarks and gluons. We will discuss the scenarios more closely.

3.1.1 High temperature phase transition

We will consider the case of the system consisting of quarks and gluons with zero net baryon content at very high temperature T contained in volume V. We can greatly simplify the problem by setting the particles to be noninteracting and massless. We can now calculate partial pressures arising from quarks, antiquarks and gluons. It can be shown[15] that the equation of state for ideal gas of massless particles is

$$P = \frac{1}{3}\frac{E}{V} = \frac{\epsilon}{3}, \tag{3.2}$$

where ϵ is the energy density.

For massless particles at temperature T the distribution of the states of momentum p in volume V is

$$\frac{dN}{dp} = \frac{gV4\pi p^2}{(2\pi)^3}\left(\frac{1}{e^{(p-\mu)/T} \pm 1}\right), \tag{3.3}$$

where the $+$ sign stands for fermions and the $-$ sign for bosons and μ is the chemical potential of the given particle. Since we have the same number of quarks and antiquarks, we set $\mu = 0$. At last, the g is the degeneracy of the given particle species.

The energy of the massless quarks in this system is then

$$E_q = \int_0^\infty \frac{dN}{dp} p\, dp = \frac{g_q V}{2\pi^2}\int_0^\infty \frac{p^3\, dp}{e^{p/T}+1} = \frac{7}{8} g_q V \frac{\pi^2}{30} T^4. \tag{3.4}$$

By substituting in 3.2, we get the pressure exerted by the quarks as

$$P_q = \frac{7}{8} g_q V \frac{\pi^2}{90} T^4. \tag{3.5}$$

We can obtain in the same way the pressure from the antiquarks

$$P_{\bar{q}} = \frac{7}{8} g_{\bar{q}} V \frac{\pi^2}{90} T^4. \tag{3.6}$$

Since the degeneracy numbers are the same for quarks and antiquarks

$$g_q = g_{\bar{q}} = (colors) \times (spin\ states) \times (flavors) = 3 \times 2 \times 3, \tag{3.7}$$

we get from 3.5 and 3.6 the pressure exerted by the fermions

$$P_f = P_q + P_{\bar{q}} = \frac{7}{20} \pi^2 T^4. \tag{3.8}$$

Next we get similarly the pressure due to the gluons by using Bose-Einstein's statistic instead of Dirac's. The gluon energy is

$$E_{gl} = \int_0^\infty \frac{dN}{dp} p\, dp = \frac{g_{gl} V}{2\pi^2} \int_0^\infty \frac{p^3\, dp}{e^{p/T} - 1} = g_{gl} V \frac{\pi^2}{30} T^4. \tag{3.9}$$

The degeneracy number of gluons g_{gl} is

$$g_{gl} = (colors) \times (polarisations) = 8 \times 2. \tag{3.10}$$

Using again the 3.2 and 3.9 the pressure due to the gluons is

$$P_{gl} = \frac{16}{90} \pi^2 T^4. \tag{3.11}$$

The total outward pressure inside the bag is then

$$P = \frac{47.5}{90} \pi^2 T^4. \tag{3.12}$$

By setting the pressure P equal the bag pressure B in 3.12 we obtain the *critical temperature* of the phase transition

$$T_c = \frac{90}{47.5\pi^2} B^{1/4}. \tag{3.13}$$

From the previous estimate of $B^{1/4} = 206\ MeV$, we have $T_c \approx 136\ MeV$. As this model shows, if the temperature of the quark mass exceeds the critical temperature, the pressure of the bag will not be able to keep the quarks inside of the bag, and the quark matter will come to the deconfined phase.

3.1.2 High baryon density phase transition

The phase transition to the deconfined state of quarks and gluons is possible even at $T = 0$. In this case the pressure inside the bag will arise only from the quarks as a result of the Pauli's exclusion principle. Since the quarks are fermions they cannot populate the same states. The number of quarks populating a state with the same momenta depends on the *degeneracy number* of quarks. In the dense matter the quarks have to populate states of higher momenta to satisfy the Pali's principle. This mechanism increases pressure of the gas as the density of the gas increases. When the pressure of the degenerate quark gas reaches the bag pressure B the matter will change into the unconfined phase. Since each quark carries baryon number 1/3, the high density of quarks corresponds to the highly baryon dense matter. Note that there will be no pressure, in this case of $T = 0$, from gluons. Since gluons are bosons, they can all populate the lowest momentum state.

To calculate the pressure resulting from the degenerate quark gas we will use the distribution of quarks in the form of:

$$\begin{array}{rcll} \frac{dN}{dp} & = & \frac{g_q V 4\pi p^2}{(2\pi)^3} & \text{for } p \in \langle 0, \mu_F \rangle \\ & = & 0 & \text{for } p > \mu_F \end{array} , \tag{3.14}$$

where the μ_F is the Fermi momentum of the highest occupied state. To calculate the *critical density* we need the number of quarks N_q inside of the volume V

$$N_q = \int_0^\infty \frac{dN}{dp}\ dp = \int_0^{\mu_F} \frac{g_q V 4\pi p^2}{(2\pi)^3}\ dp = \frac{g_q V}{6\pi^2}\mu_F^3. \tag{3.15}$$

The energy E_q of the gas in volume V is

$$E_q = \int_0^\infty \frac{dN}{dp} p\ dp = \int_0^{\mu_F} \frac{g_q V 4\pi p^3}{(2\pi)^3}\ dp = \frac{g_q V}{8\pi^2}\mu_F^4. \tag{3.16}$$

Using 3.2 one can obtain the outward pressure due to quarks as

$$P_q = \frac{g_q}{24\pi^2}\mu_F^4. \tag{3.17}$$

As previously stated the phase transition will occur when the outward pressure P exceed the pressure B of the bag. The *critical Fermi momentum* $\mu_F^{critical}$ is then

$$\mu_F^{critical} = \left(\frac{24\pi^2}{g_q}\right) B^{1/4}. \tag{3.18}$$

From this we can easily get the formula for the needed *critical baryon number density* $n_B^{critica}$

$$n_B^{critical} = \frac{1}{3}\frac{N_q}{V} = \frac{4}{3}\left(\frac{g_q}{24\pi^2}\right)^{1/4} B^{3/4}. \tag{3.19}$$

After the same substitutions, as in the previous chapter, we get the estimate of the critical baryon density at the temperature $T = 0$

$$n_B^{critical} \approx 0.80/fm^3. \tag{3.20}$$

In normal nuclear matter the baryon number density is $n_B = 0.14/fm^3$. That means that the critical density is about 5 to 6 times the density of the normal matter. If the density of baryons exceeds the $n_B^{critical}$, the bag pressure will not be strong enough to sustain the pressure from quarks due to their degeneracy. The containment of quarks inside of hadrons will not be possible anymore.

3.1.3 Phase transition - general case

In previous sections 3.1.1 and 3.1.2 we have discussed two extreme scenarios under which the phase transition from hadronic mater to QGP can occur. In the first case, in section 3.1.1, the temperature is very high and the baryon net density is zero. The second, opposite case, discussed in section 3.1.2, is a case of zero temperature and high baryon density.

However it is very likely that any prepared system will lay somewhere between these two extreme cases. In such a case the pressure will arise from both, the thermal motion and the degeneracy of the fermions. The total pressure will be the sum of both contributions. All the possible scenarios can be seen in the phase diagram of the temperature and baryon density, as shown in the Figure 3.2 taken from [13]. The diagram shows also a schematic overview of different regions explored by different experimental facilities.

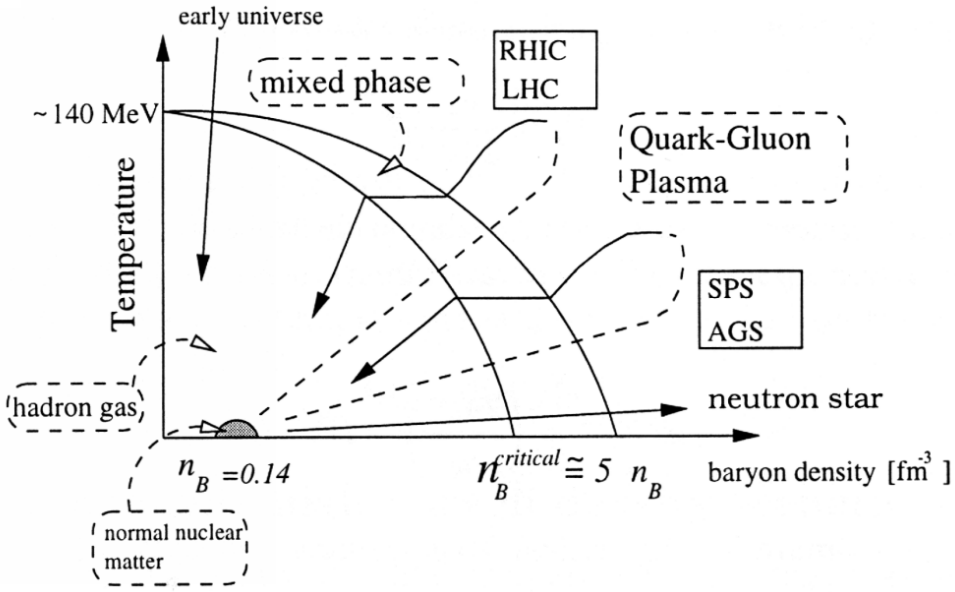

Figure 3.2: Phase diagram scenarios in different experiments.

Chapter 4

The signals of QGP and observables

Heavy-ions experiments are designed to measure number of different observables. It's unlikely that the conclusive evidence of a formation of the QGP could be based on a single observable. Instead of that simultaneous observation of many signals will be required. It is expected that only consistent analysis of many signal can lead to an unambiguous identification of the phase transition. Many of the measured signals are only indirect, because they are related to particles that undergo many reinteractions from the time of the early collision to the time of the final detection.

In the following section are discussed the most important and promising measurable signals of different parts of the ultrarelativistic heavy-ions collision and possible QGP phase transition.

4.1 Electromagnetic probes

Electromagnetic probes, like photons and dilepton pairs[17], are very good probes. Since they interact only electromagnetically, their mean free path is much larger than the collision region. They can be good probes for the very early and hot phases, because they can escape from the system without being influenced by the hadronization stage.

This ideal case is however little complicated by the existence of other background sources that can produce photons and dileptons before, or after the hot stage of the collision. The interpretation of the signal is then com-

plicated by having to distinguish the contributions from different sources.

The electromagnetic emission of real or virtual photons from the plasma is the only direct observable signal for the study of the quark-gluon plasma stage.

4.1.1 Dilepton production

In the deconfined phase of quark-gluon plasma, quark can electromagnetically interact with an antiquark creating a virtual photon γ^*. This photon will then decay into a lepton-antilepton pair. The Feynmann diagram of the reaction $q + \bar{q} \to l^+ l^-$ is shown in the Figure 4.3.

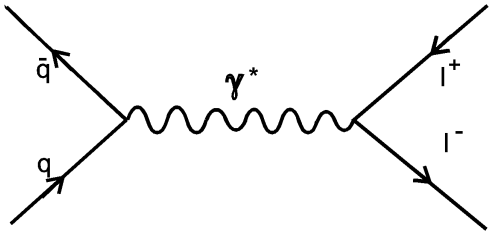

Figure 4.1: The Feynmann diagram for the reaction $q + \bar{q} \to l^+ + l^-$.

The system of the produced $l^+ + l^-$ pair (dilepton) is characterized by the invariant mass $M^2 = (l^+ + l^-)^2$, dilepton four-momentum $P = (l^+ + l^-)$ and the dilepton transverse momentum $P_\perp = (l^+_\perp + l^-_\perp)$. After the pair of l^+ and l^- is produced, both particles have to pass trough the collision region where they can interact only weakly or electromagnetically. Since the cross section for an interaction between another charged particles behaves like α^2/s, it is unlikely that the leptons would suffer another interaction before leaving the region.

The production rate and the momentum spectrum of the produced dilepton pairs, as shown in [12], depends on the momentum distributions of quarks and antiquarks in the plasma. For this reason the dileptons are suitable to probe the thermodynamical conditions in the plasma.

There are however other processes that can produce dileptons and thus blur the signal from QGP.

An important contribution to dilepton production comes from the *Drell-Yan process*[12]. In this process, as shown in the Figure 4.2, in nuclear

collision, a valence quark of a nucleon of one nucleus interacts with a sea antiquark of a nucleon of the other nucleus. The quark and antiquark annihilate into a virtual photon which then decays to l^+l^- pair. This process is most important for large values of the invariant mass of the dilepton pair.

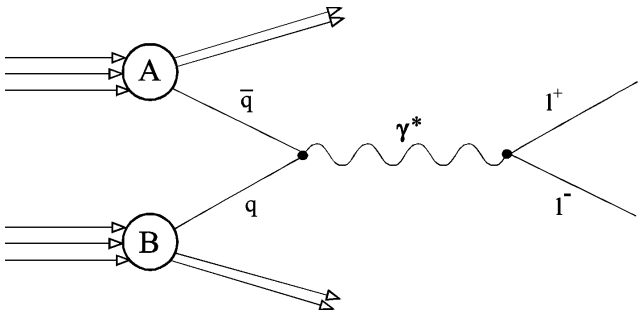

Figure 4.2: The diagram of the Drell-Yan process leading to the production of a dilepton pair.

Another contribution to the dilepton spectrum comes from the *decays of hadrons and resonances.* Dileptons can be produced in processes like $\pi^+ + \pi^- \to l^+ + l^-$ or by decays of hadron resonances such as ρ, ω, and J/ψ.

Hadrons and resonances are produced mainly in the initial collision. After the chemical freeze-out, the interacting hadronic gas can also produce same resonances. The dileptons coming from decays of hadron resonances will manifest themselves as peaks in the invariant mass spectrum of the $l^+ + l^-$ pairs with the width corresponding to their mean life time.

4.1.2 Photons

In the quark-gluon plasma the source of real photons are mainly two interactions:

1. $q + \bar{q} \to \gamma + g$ annihilation
2. $q + g \to \gamma + q$ Compton process

There is also the $q + \bar{q} \to \gamma + \gamma$ interaction, but the total cross section is much smaller then for the previous two processes.

The photons produced in the QGP are mixed with photons from other background sources. Those are mainly photons from the initial interaction of the incoming partons, photons from the decays of produced π^0 and η. There are also photons from the reactions like $\pi\pi \rightarrow \rho\gamma$, $\pi\rho \rightarrow \pi\gamma$ or decays $\rho \rightarrow \pi\pi\gamma$, taking place after the hadronization of QGP, inside the transversely expanding hadronic gas. In order to interpret right the signal from photons it is necessary to know well the signal of this background.

4.2 Strangeness enhancement

Enhanced strangeness production is another signal from the QGP[12]. If the plasma reaches the thermal equilibrium, the expected temperature is about 150-200 MeV. In a plasma the mass threshold to produce $s\bar{s}$ pair is lower than in a hadron gas, where usually the ΛK and $K\bar{K}$ pairs are created ($E > 700MeV$). The s quark will, with high probability, combine with other quarks creating a baryon and the antiquarks $\bar{s}$ will combine with a quark to create a meson. This all will lead to an enhanced production of strange particles like Λ and K^+. Also, as the baryon density increases and the light quarks have to populate states with higher energies, it's getting more favorable to produce the strange quarks. More about the strangeness production at RHIC can be found in [18].

4.3 J/ψ suppression

J/ψ suppression signal, as predicted in [16], tests the production of the charmonium in the heavy-ion collisions. If nuclear collisions lead to the formation of the deconfined quark-gluon plasma, the color charge of quarks is screened by the Debye screening, similarly as in the QED [19]. Since the linear confining part of the strong force potential vanishes in the QGP, there remains only phenomenological Coulombic potential between the quarks. This potential is changed due to Debye screening of color charge as

$$V_{qq} \approx \frac{1}{r} e^{-r/\lambda_D}, \tag{4.1}$$

where $\lambda_D = \sqrt{\frac{2}{3}}\frac{1}{gT}$, which is analogous to Debye length in QED. At high temperatures, the range of the interaction gets smaller than the distance

between c and $\bar{c}$ quarks in J/ψ. It's then impossible for the charmed quarks to create the bound state. The c quarks and the $\bar{c}$ antiquark will then hadronize with the light quarks and antiquarks to create 'open charm' mesons.

4.4 Jet quenching

Hard processes are mainly associated with the initial stages of the collision. The jets created in the beginning of the collision have to pass trough the medium, but are less affected by the final hadronization. These jets can be used for the study of the early parton dynamics and evolution of the QGP.

Jet quenching is studied through high $p_\perp$ hadron spectra, because high $p_\perp$ particles come from the jet fragmentation. The high energy partons producing these jets interact with the dense medium and loose energy in it. Therefore the jet quenching causes suppression of high $p_\perp$ spectra. The energy-loss of the partons in the dense matter is very sensitive to the density and can thus be used as a probe of the dense matter created in the ultrarelativistic collisions.

4.5 Single particle spectra

The study of single particle spectra and ratios of different particles can provide informations about the degree of thermal and chemical equilibrium reached in the evolution after the collision. For such analyses mainly the transversal components of the momenta or masses are considered, because they are stripped off the non-thermal components. With these analyses one can obtain informations about the collective motion called the *"transversal flow"*[13].

4.6 HBT interferometry

Classical interferometry is based on the superpositions of amplitudes of two or more physical waves. Examples of such an interferometry can be found in mechanics or optics. However in *Hanbury-Brown Twiss interferometry* it is not the amplitudes, but the intensities that are superposed. It is a quantum mechanical effect. Instead of measuring the amplitude of an observable

at one point in the space, we measure the interference of probability amplitudes for finding two identical particles at two different space-time or energy-momentum points. This technique was first used in 1956 in astrophysics by Hanbury-Brown and Twiss[32] for measuring the angular diameter of a star.

What is measured is the correlation in space-time or energy-momentum for two *identical* particles (the *HBT effect*) that comes from the symmetrization of a wave function of bosons (*Bose-Einstein effect*), or antisymmetrization in the case of fermions (*Fermi-Dirac effect*). The size of the correlation depends on the size and properties of the emitting source.

For a simplified description we will follow the approach described in [12]. More detailed description of this method and it's application in the relativistic heavy-ion physics can be found in [27].

First we need the probability amplitude $\Psi(k : x \to x')$ for a particle with a four-momentum k to be produced at a space-point x and detected at x'. For a particle moving along it's classical trajectory it can be calculated as

$$\Psi(k : x \to x') = A(k, x)e^{i\phi(x)}e^{ik\cdot(x-x')}, \tag{4.2}$$

where $A(k, x)$ is a probability amplitude for the production of a particle with four-momentum k at x. The $\phi(x)$ is a production phase. The particle can be produced from the whole source, we thus have to sum over the source:

$$\Psi(k : \{source\} \to x') = \sum_{source\ x} A(k, x)e^{i\phi(x)}e^{ik\cdot(x-x')}. \tag{4.3}$$

If the source has continuous space-time density $\rho(x)$the summation in 4.3 changes to an integral over x

$$\sum_{source\ x} \ldots \quad \to \quad \int_{source} dx\ \rho(x) \ldots\ . \tag{4.4}$$

Now let's consider two identical bosons, with a four-momenta k_1 and k_2, emitted from the source, and detected at space-time points x_1' and x_2'. Because of indistinguishability of the bosons and the Bose-Einstein statistics of identical bosons, the probability amplitude Φ must be symmetrical with respect to an interchange of the particles. After this symmetrization we get

$$\begin{aligned}
\Phi &= \frac{1}{\sqrt{2}}\{A(k_1, x_1)e^{i\phi(x_1)}A(k_2, x_2)e^{i\phi(x_2)}e^{ik_1\cdot(x_1-x_1')}e^{ik_2\cdot(x_2-x_2')} \\
&\quad +A(k_1, x_2)e^{i\phi(x_2)}A(k_2, x_1)e^{i\phi(x_1)}e^{ik_1\cdot(x_2-x_1')}e^{ik_2\cdot(x_1-x_2')}\} \\
&\equiv e^{i\phi(x_1)}e^{i\phi(x_2)}\Phi(k_1k_2 : x_1x_2 \to x_1'x_2'),
\end{aligned} \tag{4.5}$$

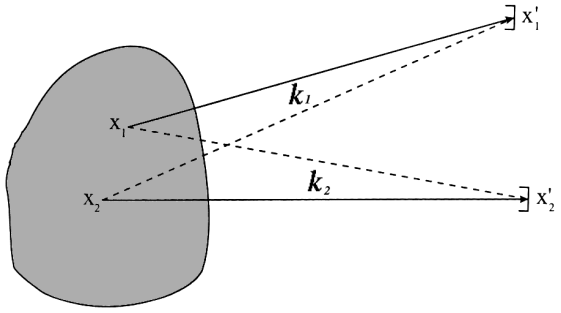

Figure 4.3: A boson of momentum k_1 is detected at x_1' and another identical boson with momentum k_2 is detected at x_2. Since we cannot distinguish the particles from each other, we have to consider a superposition of both trajectories.

where $\Phi(k_1 k_2 : x_1 x_2 \to x_1' x_2')$ does not depend on the production phase ϕ. The total amplitude is then again a summation over the whole source:

$$\Psi(k_1 k_2 : \{source\} \to x_1' x_2') = \sum_{x_1, x_2} e^{i\phi(x_1)} e^{i\phi(x_2)} \Phi(k_1 k_2 : x_1 x_2 \to x_1' x_2'). \quad (4.6)$$

The two-particle momentum distribution $P(k_1, k_2)$ is then given by

$$P(k_1, k_2) = \frac{1}{2} \left| \Psi(k_1 k_2 : \{source\} \to x_1' x_2') \right|^2 . \quad (4.7)$$

An important assumption that has to be made is about the production phases ϕ of the source. If we suppose that the source is chaotic, which means that the production phase is random, the 4.7, as shown in [12], simplifies to

$$P(k_1, k_2) = \left| \Phi(k_1 k_2 : \{source\} \to x_1' x_2') \right|^2 . \quad (4.8)$$

This can be written in the form of integral

$$P(k_1, k_2) = \int_{source} dx_1 dx_2 \; \rho(x_1)\rho(x_2) \left| \Phi(k_1 k_2 : \{source\} \to x_1' x_2') \right|^2 . \quad (4.9)$$

After some manipulation we get

$$P(k_1, k_2) = P(k_1)P(k_2) + \left| \int dx \; \rho(x) A(k_1, x) A(k_2, x) \right|^2 , \quad (4.10)$$

where $P(k)$ is a single particle momentum distribution. After some renaming, we get from 4.10

$$P(k_1, k_2) = P(k_1)P(k_2)\left(1 + \left|\int dx\ e^{i(k_1-k_2)x}\rho_{eff}(x, k_1, k_2)\right|^2\right), \qquad (4.11)$$

where ρ_{eff} is the *effective density*

$$\rho_{eff}(x, k_1, k_2) = \frac{\rho(x)A(k_1, x)A(k_2, x)}{\sqrt{P(k_1)P(k_2)}}. \qquad (4.12)$$

The Fourier transform of $\rho_{eff}(x, k_1, k_2)$ is

$$\tilde{\rho}_{eff}(q, k_1, k_2) = \int dx\ e^{iqx}\rho_{eff}(x, k_1, k_2), \qquad (4.13)$$

where $q = k_1 - k_2$. The two-particle distribution function $P(k_1, k_2)$ from 4.11 changes to

$$P(k_1, k_2) = P(k_1)P(k_2)\left(1 + |\tilde{\rho}_{eff}(q, k_1, k_2)|^2\right), \qquad (4.14)$$

What we measure, is the correlation function defined as

$$C_2(\vec{p_1}, \vec{p_2}) = \frac{P(\vec{p_1}, \vec{p_2})}{P(\vec{p_1})P(\vec{p_2})}. \qquad (4.15)$$

From 4.11 we have

$$C_2(\vec{p_1}, \vec{p_2}) = 1 + |\tilde{\rho}_{eff}(q, k_1, k_2)|^2. \qquad (4.16)$$

From 4.16 we see that, for the chaotic source, the two-particle correlation function for bosons $C_2(\vec{p_1}, \vec{p_2})$ is related to the Fourier transform of the effective density.

A typical correlation function C_2 is shown in the Figure 4.4. This figure was taken from [20].

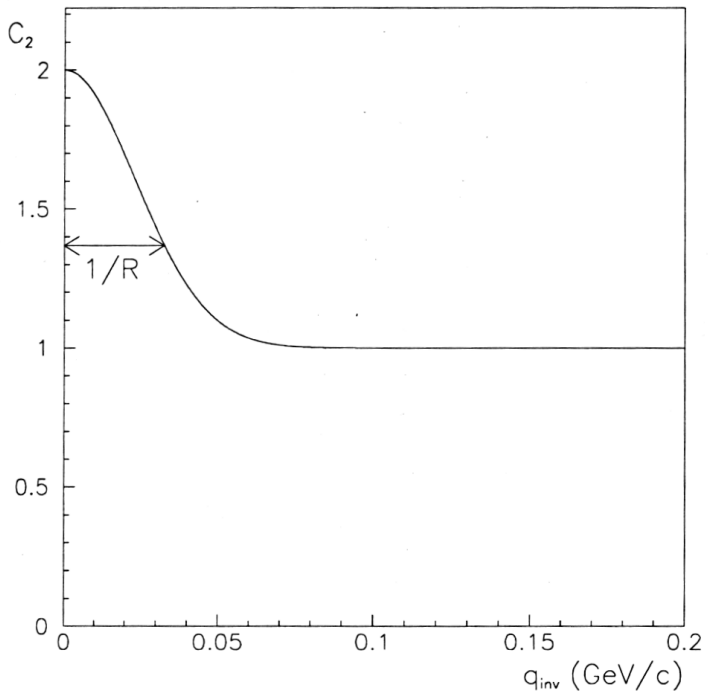

Figure 4.4: Two-particle correlation function of a source with a typical length scale R of 6 fm. Figure from [20]

Chapter 5

Silicon Vertex Tracker at STAR

5.1 STAR

The STAR[22] stands for **S***olenoidal* **T***racker* **A***t* **R**HIC. The baseline configuration of the STAR detector consists of a system of subdetectors inside of a large room temperature solenoidal magnet. The schematic drawing of the detector is shown in the Figure 5.1. The main detector is the Time Projection Chamber (TPC)[21]. The TPC tracks charged particles with the pseudorapidity $|\eta| < 1.8$ for collisions in the center of the TPC with full azimuthal coverage. The TPC is placed in the magnetic field of strength of $\pm 0.25\ T$ or $\pm 0.5\ T$, allowing tracking of particles with momenta $p_\perp > 75 MeV/c$. A typical central collision at $\sqrt{S_{NN}} = 200\ GeV$, as it was recorded in the TPC, is shown in the Figure 5.2.

The central trigger barrel (CTB) is an array of scintilator slats which is arranged around the TPC. The CTB is used for measuring the multiplicity of charged particles streaming from the collision. Because of it's fast response it is used in the *level 0 triggering*. Another detector used for triggering together with the CTB is the Zero degree calorimeter (ZDC). There are two ZDC located at $\pm 18m$ from the detector center. They are placed at $|\sin\theta| < 0.002$. That allows them to detect the fragmentation neutrons from the collision and measure their energy. The signal from ZDCs is used in the coincidence with the CTB for triggering. Both the ZDCs and CTB can be used for computing the centrality of the event.

To detect particles that emerge under small angles and cannot thus be detected by TPC two Forward time projection chambers (FTPC) are installed

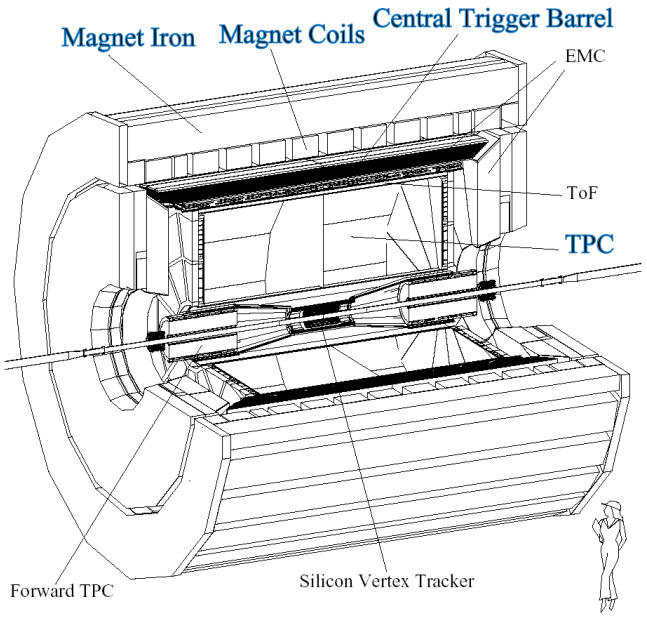

Figure 5.1: Schematic view of the STAR detector.

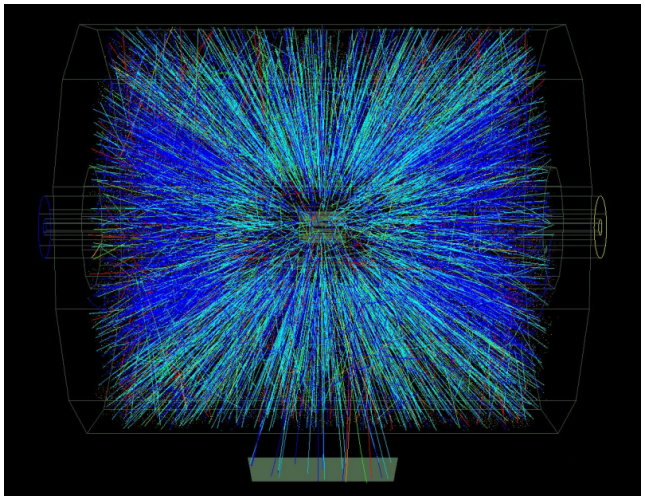

Figure 5.2: Tracks of charged particles from a central collision of two gold atoms at $\sqrt{S_{NN}} = 200\ GeV$ that were recorded by the Time Projection Chamber of STAR.

at the sides of the detector. They differ from the main TPC not only in the size, but also by the direction of the drift. While in the main TPC the drift is longitudinal along the beam pipe, in the FTPCs the drift is diagonal, perpendicular to the beam pipe.

In the 2001 year run there were also installed first slats of the Electromagnetic calorimeter (EMC). These first parts were for testing purposes, but during this years upgrade the whole calorimeter will be placed inside. The EMC is positioned between the TPC and the coils of the magnet. During the upgrade period a new end-cap calorimeter will be placed in the detector. Also the vertex detector will be enhanced by one layer of a silicon strip detector.

5.2 SVT

One of the STAR detectors is the Silicon Vertex Tracker (SVT)[23, 24]. With only the TPC, STAR can detect only particles with $p_\perp > 75\ MeV/c$, and has thus a limited accuracy and efficiency for the study of short lived particles that decay before they reach the inner layer of the TPC. Multi-strange baryons cannot be studied using only the TPC.

The SVT detector enhances STAR capabilities for particle identification and momentum resolution, and extends the detectors acceptance for low $p_\perp$ phenomena. It offers unique capabilities for the study of strange and multi-strange particle production and makes possible the HBT interferometry using neutral particles. The SVT can also be used in the algorithms of the third level triggering. The most important improvements in the STAR physics capabilities due to the SVT are the following:

Flavor physics

One of the signs of the formed QGP might be the enhancement of the relative abundance of strange to non-strange quarks[12][26]. The addition of the SVT, with its high position resolution close to the production vertex, allows the elimination of most of the combinatorial background and greatly improves the detection efficiency for strange particles.

Low $p_\perp$ physics

Enhancements in the low momentum part of invariant cross section spectra were discovered in heavy-ion reactions at CERN and AGS. The phenomena related to pion $p_\perp$ spectra under $200 MeV/c$ is not fully understood. Results from AGS for low $p_\perp$ kaons also reveal a very steep component at very low $p_\perp$ (below $50 MeV$) which might be linked to QGP production. The high position resolution and low $p_\perp$ acceptance of the SVT for pions, kaons and protons is mandatory for the these studies.

HBT interferometry with neutral particles

Measurements of the two-particle Bose-Einstein correlations can be interpreted in terms of the space-time structure of the emitting source and can provide a signature of the QGP formation[27]. Kaon interferometry offers significant advantages over pions with respect to the final state interactions and resonance formation, which obscure the interpretation of the measured data. The SVT is essential for the K^0_S interferometry, because it enables efficient secondary vertex reconstruction.

Other SVT capabilities

The Svt also enhances the capabilities of STAR detector in areas where the TPC performance is improved by combining the SVT and TPC measurements.

Primary track reconstruction: The SVT extends range of primary particle reconstruction and also enhances the tracking efficiency for momenta below $400 MeV/c$.

Particle identification: The good dE/dx resolution of the SVT complements the identification capabilities of TPC. Addition of SVT extends the upper limit for K - π separation to about $600 MeV/c$ and for p - π to about $800 MeV/c$.

Two-track resolution: HBT analyses depend on the ability to separate tracks with small relative momenta. The improved two-track resolution of the SVT-TPC system can increase the maximum source size to which STAR is sensitive.

Secondary track reconstruction: The position of the SVT close to the primary vertex enhances identification and reconstruction of decay vertices.

High $p_\perp$: At high $p_\perp$ the momentum resolution of TPC is restricted by it's position resolution ($\approx 700\mu m$), which limits the determination of the curvature of these nearly straight tracks. SVT provides accurate position information near the main vertex, thus improving the resolution for high $p_\perp$.

Primary vertex location: The SVT improves the main vertex position resolution. That is especially useful in low multiplicity events. It should also enhance the ability to reject multi-vertex events.

Triggering: The SVT provides the third level trigger capabilities. It is possible to access particle spectra within a few tens of milliseconds. This makes possible to trigger on, for example, particle ratio fluctuation or low momentum enhancement.

5.3 General principles of silicon drift detectors

Silicon drift detectors (SDDs) could very shortly be described as "solid state TCPs". These detectors combine some of the main advantages of the normal gas drift chambers (like the small number of readout channels) and the advantages of solid state detector (such as the excellent position and energy resolution). They operate in a fashion similar to conventional drift chambers, but the gas is replaced by n-type silicon, as first proposed by Rehak and Gatti[28].

Schematic drawing of the silicon drift detector is shown in the Figure 5.3.

The detector is made of thin n-type semiconductor wafer of a thickness of 300 μm. There are $P+$ cathode strips implanted symmetrically on both sides of the wafer. At the edge of the wafer are placed $N+$ segmented anodes of a size 200 $\mu m \times 200$ μm at a pitch of 250 μm.

When a charged particle passed trough the detector, it ionizes a small region. The free electrons then drift inside of the n-type bulk to the anodes at the end. The electrons are kept in the bulk and directed toward the anode by an external field created by the implanted $P+$ cathodes. The *drift velocity* of electrons inside the silicon[30] is

$$v_{drift} = \mu E, \tag{5.1}$$

where v_{drift} is the drift velocity, μ is the *electron mobility* and E is the electric field. If the bulk of the silicon is without non-uniformities in doping,

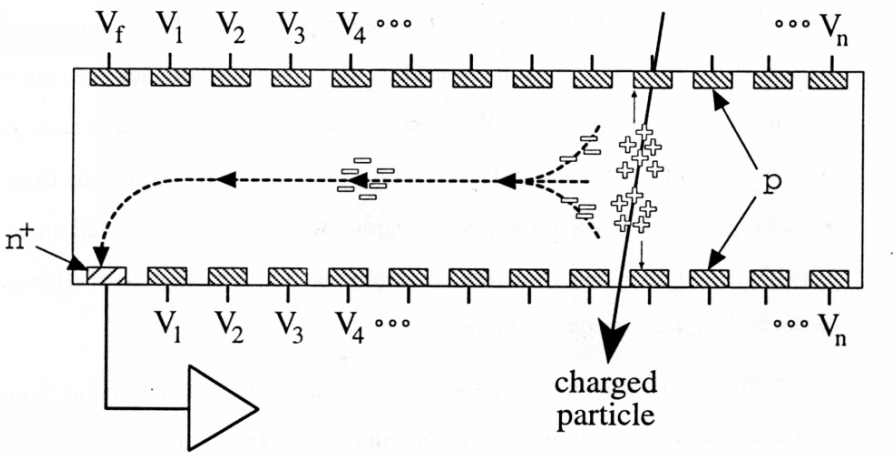

Figure 5.3: Schematic principle of the silicon drift detector. Figure from [29].

the electron mobility is constant. If a constant electric field is applied then the drift velocity is constant as well. Thus from measuring the drift time it is possible to calculate the drift distance. From this point of view the whole detector can be divided into two parts: the *drift region* (most of the detector) and the *focusing region* (around the collecting anodes). The position of the hit on the axis perpendicular to the drift is measured by the position of the anode that collected the drifting charge. As the cloud of the electrons drifts toward the anodes it spreads due to the diffusion and Coulombic repulsion. This causes the signals to appear on more that one anode. The exact position of the hit can be calculated from the distribution of the charge with better precision than is the pitch o the anodes. The expected position resolution along the anodes is about $25\mu m$.

5.3.1 p-n-p junction potential

The detector can be seen as two back-to-back p-n junctions[30]. It's thus important to understand the function of the p-n junction in order to describe the bulks depletion and the creation of the drift field. The p-n junctions are operated at reverse bias. This creates a region depleted of mobile charge carriers, which is the active region of the detector. As the reversely biased potential is increased the depletion zone extends deeper into the silicon. If we consider the junction to be infinitesimally small, the potential around the

p-n junction and the depth of the depletion region can be calculated using the Poisson's equation in the n-type

$$\frac{d^2V_n(x)}{dx^2} = -\frac{eN_d}{\epsilon} \tag{5.2}$$

and p-type silicon

$$\frac{d^2V_p(x)}{dx^2} = -\frac{eN_a}{\epsilon}, \tag{5.3}$$

where e is the electron charge, ϵ is the dielectric constant in silicon and the N_d and N_a stand for the concentration of donors and acceptors. The silicon is doped with donors where $x > 0$ and acceptors where $x < 0$.

The depth of depletion W_n and W_p in the n-type and p-type silicon layer depends on the boundary condition for the electric field E and the potential. If the n-type side is held at the ground potential and at the p-type side is applied biased potential $-V_{bi}$, the boundary conditions for electric field are $E(W_n) = 0$, $E(W_n) = 0$ and for the potential $V_n(W_n) = 0$, $V_p(-W_p) = -V_{bi}$. The equations 5.2 and 5.3 then give the potentials

$$V_n(x) = -\frac{eN_d}{2\epsilon}(x - W_n)^2 \tag{5.4}$$

$$V_p(x) = \frac{eN_a}{2\epsilon}(x + W_p)^2 - V_{bi}. \tag{5.5}$$

At the junction ($x = 0$) the potentials V_n and V_p must be equal. Considering also that the overall net charge must be zero, from which follows

$$N_d \cdot W_n = N_a \cdot W_p, \tag{5.6}$$

it is possible to get the total depth of the depleted region $W_{total} = W_p + W_n$

$$W_{total} = \sqrt{\frac{2\epsilon}{e}\frac{N_a + N_d}{N_a N_d}|V_{bi}|}. \tag{5.7}$$

The silicon used for SVT has the donor doping of $1.0 \times 10^{12}\ cm^{-3}$ for the n-type bulk and acceptor doping of $1.0 \times 10^{18}\ cm^{-3}$ for the p-type cathodes. The equation 5.7 can thus be approximated as

$$W_{total} = \sqrt{\frac{2\epsilon|V_{bi}|}{eN_a}}. \tag{5.8}$$

As previously stated, the detector can be considered as two back to back junctions. If there is no voltage applied, the depleted region is only under the p-type cathodes leaving the rest of the n-type bulk conductive. This conductive area can carry thermally generated electrons that create the noise in the detector. By increasing the potential at both p-type sides the depleted region can be extended further to the n-type bulk. With a sufficiently large potential the whole detector can be fully depleted as shown in the Figure 5.4. Since the doping of the p-type side is much bigger, the cathodes can be quite small, and the main part of the depleted area is the n-type bulk. With this potential, any electrons created by incident particles inside of the depleted region will be confined in the middle of the silicon bulk.

In order to read the signal, the created electrons have to be brought to the collecting anodes at the end of the wafer. This is made possible by superimposing a linear potential, parallel to the surface, with the parabolic potential that holds the electrons in the bulk. The linear potential is created by gradual increase in the bias potential on the cathodes on both sides of the wafer. This creates the linear electric field in the drift direction. Typical field strengths used for drift detectors are from about 200 V/cm to 800 V/cm.

In the focusing region of the detector the drifting cloud of the electrons has to be brought to the surface to the collecting anodes. This is done by applying different bias potentials at opposite sides of the wafer. The minimum of the potential valley is this way gradually shifted from the center of the bulk toward the anode. The shape of the potential inside of the detector in the drift region and in the focusing region is shown in the Figure 5.5 and the Figure 5.6 .

5.4 Silicon drift detectors in heavy-ion physics

The properties of the silicon drift detectors make these devices suitable for the use in the heavy-ion experiments. The SDDs give 2-dimensional information with a comparable precision to the strip detectors. They are capable to handle high multiplicity events. Their main advantage, when compared to other semiconductor detectors with comparable precision, comes from the low number of readout channels. The number of readout channels and front-end electronics grows linearly with the covered area ,instead quadratically, like in the case of pixel detectors. They are thus much cheaper then pixel and also strip detectors.

On the other hand, there are some drawbacks connected with this design. Since the electrons have to travel trough the whole detector before they are detected, the detector is slower then pixel detectors. It takes about 5 μs to read out the detector. The detector cannot thus be used for the low level triggering. Also, since the detector reads out the signal continually, the events have to triggered from outside, based on information from other detectors.

5.5 SVT setup

The SVT consists of 216 silicon drift detectors (SDDs) mounted on the three concentric barrels. Figure 5.7 shows the schematic SVT layout. Barrels consist of 6, 12 and 16 ladders which carry different number of SSDs. The detector is designed to cover pseudorapidity region $-1 < \eta < 1$ while minimizing the number of used silicon wafers. The inner layer's ladders carry 4 SDDs, the middle ones carry 6, and the outer ones carry 7 SDDs. Each barrel consists of two "sublayers" which are tiled with respect to each other to minimize dead areas. The detector has an active length of 42 cm and a diameter of 30 cm. The geometrical specifications are listed in the Table 5.1.

length of active area	42 cm (max.)
inner barrel radii	5.97 cm
middle barrel radii	10.16 cm
outer barrel radii	14.91 cm
number of wafers	216
inner barrel	32 (8×4)
middle barrel	72 (12×6)
outer barrel	112 (16×7)

Table 5.1: Specifications of the SVT.

The ladders are made of Beryllium frame to which are epoxied the silicon wafers. The front-end electronics for each ladder are epoxied on carbon-fiber electronic carrier that contains small channel trough which flows water in order to sink the heat created from the electronics. The ladders and electronic carriers are supported at each end by two Beryllium end caps.

5.6 STAR-SVT SDD design

The SDD detectors used in STAR-SVT are made of 280 μm thick silicon. The detector's size is 63 $mm \times 63$ mm. It's divided into two half-detectors with opposite direction of drift by the so called "continental divide", the central cathode that receives the maximum voltage bias. This design allows the detector to work with smaller maximum voltage. This helps to keep the drift speed constant, because in the used electric field the electron mobility is well independent of E. Also the spread of the drifting electron cloud is smaller due to the shorter drift distance. This increase of precision is at the cost of doubling the number of readout channels and electronics.

At the ends of both drift directions are the readout anodes of a size 200 $\mu m \times 200$ μm at a pitch of 250 μm. The Figure 5.8 shows a detail of a corner of the SDD. In each drift direction, there are 220 P^+ cathode strips implanted on both surfaces with a spatial pitch of 135 μm to maintain the linear drift field inside the bulk. The adjacent cathode strips are connected with the "M" shaped resistors to create the gradual decrease of the bias potential. On the lateral side the *guard lines* connect to every 10th cathode of each half-detector. These lines connect each 10th cathode of one half-detector to that of the other half. It means that only one half of the detector needs external bias, and the other half is biased automatically. The guard lines also create the necessary *guard area* that controls the voltage gradient from the high-voltage center of the detector to the sides of the silicon wafer. The guard area is minimized so that the active area of the detector covers 94.5% of the detector.

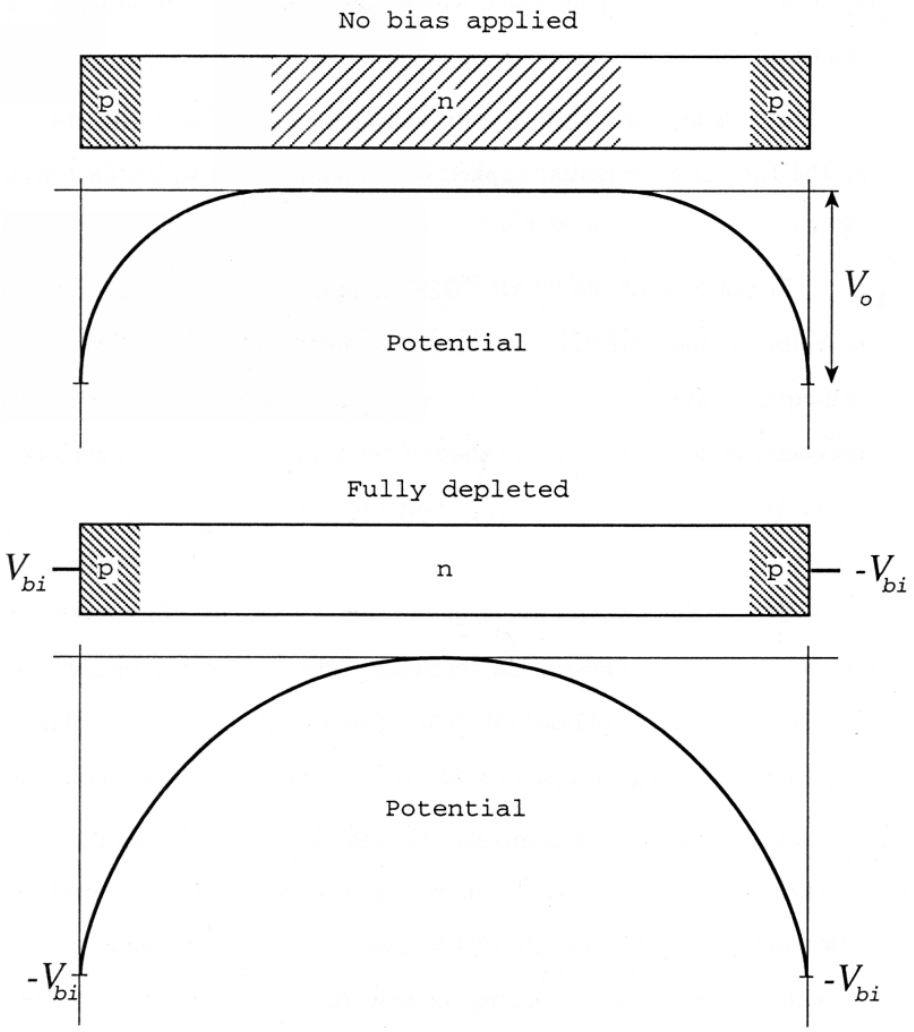

Figure 5.4: The p-n-p junction in the SDD partially and fully depleted. Figure from [29].

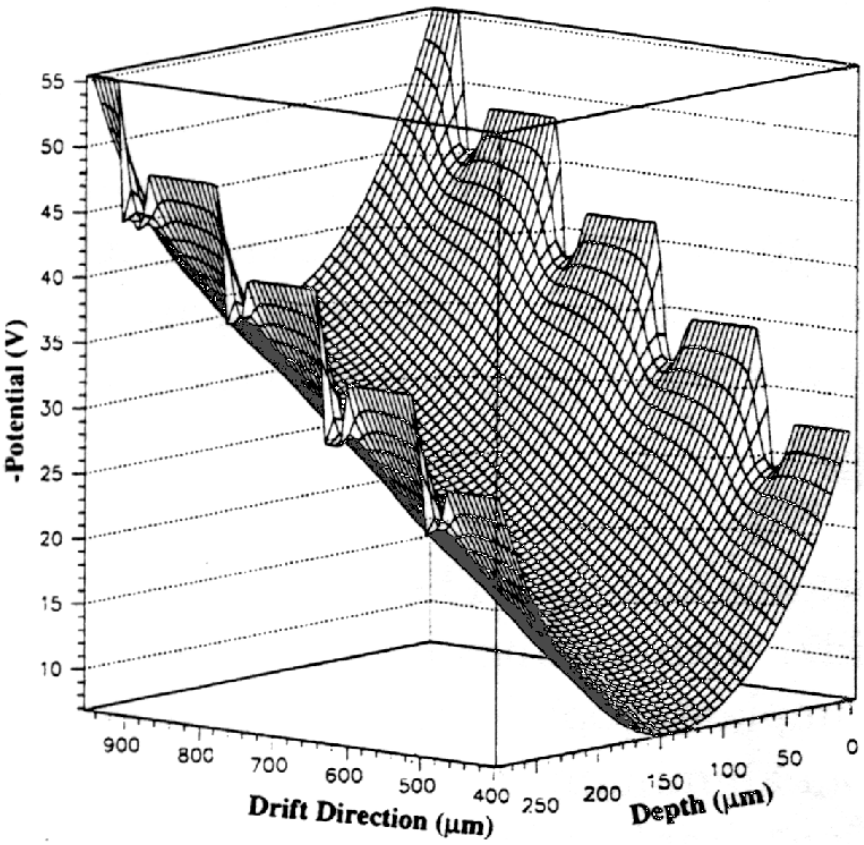

Figure 5.5: The electric potential in the drift region of the silicon drift detector.

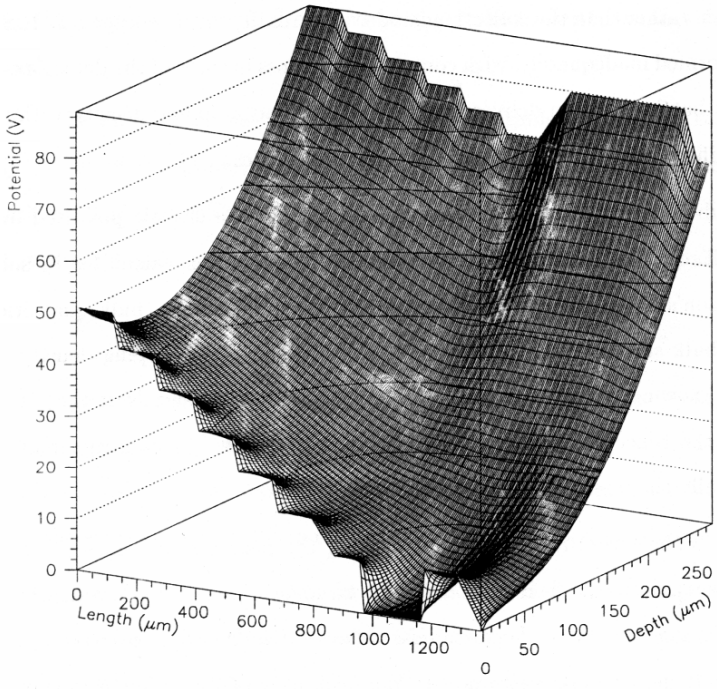

Figure 5.6: The electric potential in the focusing region of the silicon drift detector.

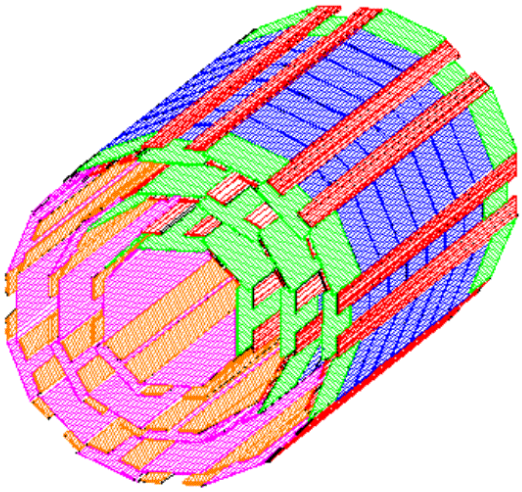

Figure 5.7: The schematic layout of the SVT.

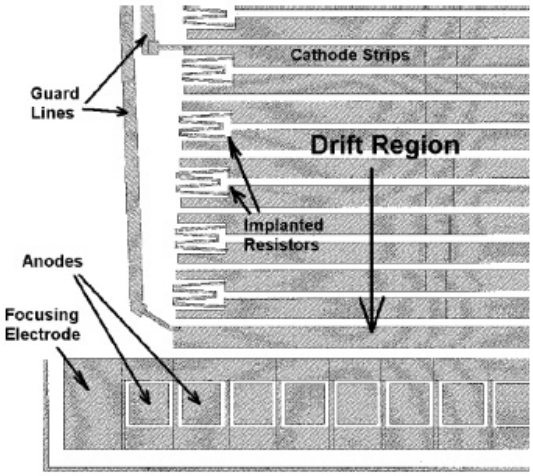

Figure 5.8: Detail view of the corner of the SDD used in STAR. Figure from [23].

Chapter 6

Drift speed calibration

For a drift detector it's important to achieve as good hit resolution as possible in the drift direction. Resolution in the drift direction is sensitive to maintaining highly linear drift field across the detector. The drift velocity depends mainly on the applied electric field, magnetic field and temperature. In this chapter we will discuss the effects of the electric field non-linearities that depend on the temperature changes.

The nominal working voltage of the STAR SDDs is $-1500\ V$ which makes an electric field of $E = 500\ V/cm$. For electric fields smaller than $1000\ V/cm$ the electron mobility μ_e can be considered independent of E. The drift velocity for the field of $E = 500\ V/cm$ is then about $6.75\ \mu m/ns$.

6.1 Drift non-linearities

6.1.1 Position dependent non-linearities

The linearity of the drift field was measured in the laboratory using laser of $\lambda = 820\ nm$ [23]. Figure 6.1a shows the measurement of the drift distance versus the drift time. Measurements were made with $100\ \mu m$ steps in the drift distance and temperature controlled to about $0.1\ K$. The measured dependence is apparently linear and can thus be fitted with a line. The deviation from the linear fit is shown in the Figure 6.1b. It can be seen from this that the main non-linearity is in the focusing region of the detector. The first approximation would be to use a function consisting of two linear function with different slopes. For better precision is necessary to use a

polynomial of higher order.

The laser measurements were made using laser corresponding to hits of about 10 MIP. To obtain the estimate of a possible achievable resolution of the SVT the whole process was repeated with 1 MIP laser hits. From these measurements, in well controlled environment, the resolution estimate is 20 and 25 μm in the anode and drift direction.

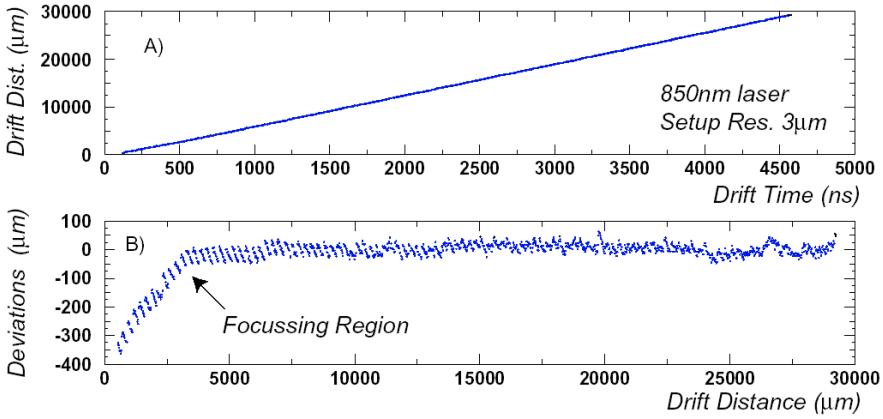

Figure 6.1: (a)Laser measurements of drift time versus drift distance; (b)difference between measured data points and a straight line fit. Figure from [24].

In order to achieve good resolution it's necessary to know well the drift velocity. Before the assembling, the whole detector was mapped using the laser in order to be able to correct for the drift field non-linearities.

6.1.2 Temperature dependent non-linearities

The electron drift mobility in the silicon depends strongly on the temperature. During the tests of the detector, temperature changes of the size of 0.1 K were measurable. At the room temperature the electron mobility is proportional to the term

$$\mu_e \approx T^{-\beta}, \tag{6.1}$$

where $\beta \approx 2.4$, when T is about 300 K. The mobility is then

$$v_e = \mu_{e0} \left(\frac{T}{T_0} \right)^{-\beta} E, \tag{6.2}$$

where $T_0 = 300\ K$, μ_{e0} is the electron mobility at T_0, and v_e is the drift velocity. This means that the time of detection, at the collecting anodes, of two hits arriving from the same position will change by Δt if the temperature changes by ΔT. For small fluctuations around the T_0 it's given as

$$\Delta t = \left(\frac{\beta}{v_e(T_0) T_0} \right) \Delta x = \left(\frac{\beta}{\mu E T_0} \right) x \Delta T. \tag{6.3}$$

If, during the reconstruction, we assume the unchanged drift velocity $v_0(T_0)$, the error of the position of the reconstructed hit is

$$\Delta x = \frac{\beta}{T_0} x \Delta T \quad \Rightarrow \quad \frac{\Delta x}{x} \sim \frac{\Delta T}{T_0}. \tag{6.4}$$

Note that the error due to the temperature fluctuations grows not only with the temperature, but also with the drift distance. Thus the SDD consisting of two half-detectors is less sensitive to temperature fluctuations. For a drift distance of 1 cm the error is $\Delta x / \Delta T = 80\ \mu m/K$ at the room temperature. The maximum drift distance at SVT is about 3 cm and the temperature fluctuations are 1 K.

From this we see that, for a good accuracy, it is necessary to control the temperature of the silicon to less then one degree, or perform an on-line drift velocity calibration. The on-line calibration can be done by injecting a charge into the bulk of the detector at an exactly specified position.

6.2 MOS injectors

In SVT the Metal-Oxide-Semiconductor structures (MOS) are used for injectors. More generally this structure is called Metal-Insulator-Semiconductor (MIS). As the name suggests, this structure is made of three layers of different materials (detailed description can be found in [30].). In our case the used metal is aluminum and the semiconductor is the n-type silicon bulk of the detector. The role of the insulator plays the silicon dioxide ($Si0_2$) layer

that was thermally grown during the detector production process. The injectors consist of a continuous aluminum line $\approx 8\ \mu m$ wide over a 3500 Å thick layer of SiO_2. These injectors make no contact with the bulk of the silicon.

At the surface, between the cathodes, is the layer of SiO_2, which traps positive charge. This charge creates potential well in the drift field close to the surface of the bulk. As show in the Figure 6.2, there are pockets in the potential close to the surface between each two adjacent cathode-lines. The detail of this pocket in the potential is in the Figure 6.2.

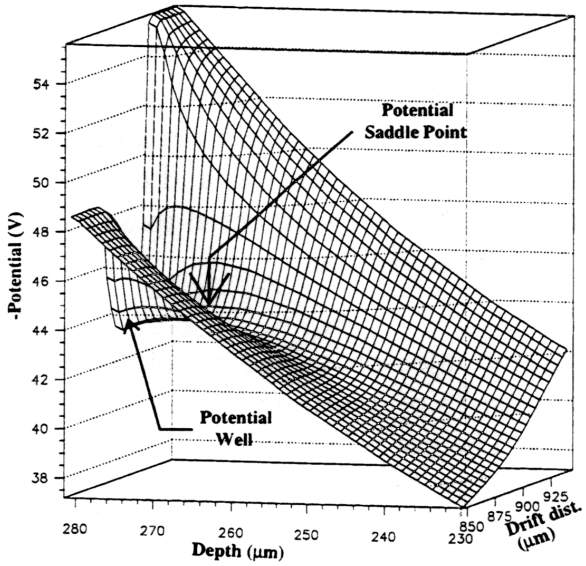

Figure 6.2: Map of the electric potential under the MOS injector.

The well is partially filled with electrons. The number of accumulated electrons is the result of a dynamical equilibrium between the number of electrons generated in the bulk and surface, and the number of electrons that escape out of the well. The MOS structure of the injector is created above this potential well. The injectors work by disturbing this equilibrium and forcing the electrons out of the well into the bulk. More about the function, design and performance of injectors can be found in [25].

Once the electrons are injected into the bulk, they drift in the mid-plane of the SDD from the injector following the same path to the collecting anodes, as would the electron cloud from a normal particle hit. They are subjected

to the same changes in the drift velocity, but the position of their origin is exactly known. They thus provide a good method for calibrating the drift velocity of the electrons in the SDD.

6.3 Injectors at SVT

The drift detectors used at SVT are equipped with total number of six MOS line injectors per detector. Two of the injectors are placed at the beginning of the wafer, at the top and bottom. These two injectors inject into the region of the collecting anodes. These are used for testing the functionality of the anodes. They should also be used to obtain the exact "t_0 position" [1]. The other four injectors are placed at different distances from the collecting anodes. The distances are listed in the Table 6.1.

Injector	Drift distance
n0	2275 μm
n1	9968 μm
n2	19698 μm
n3	29948 μm

Table 6.1: Distances of the injectors from the center of the collecting anodes.

An ideal situation would be to measure the drift time of the electrons from these injectors, and then fit the measured points with a curve that was previously measured at a fixed temperature. An example of a typical good injector event is shown in the Figure 6.3. The event is shown in the graph where x-axis represents the anodes (1 bin is 250 μm) and on the y-axis is the drift time. One time bin on the y-axis is 40 ns which corresponds approximately to 300 μm. The histogram shows the signal which depends on the amount of collected charge (the ADC value). However the injectors at the SVT do not work properly. They work irregularly, and on only few places. The injectors were designed to work with voltage pulses of about 5 V, with a possible maximum of 15 V. When the SDDs were tested, it was decided that the maximum voltage of 15 V will be used instead of the recommended

[1] Because the readout of the detector is continuous the recording of event has to be triggered from outside. t_0 is the position in the drift region where the recorded event starts.

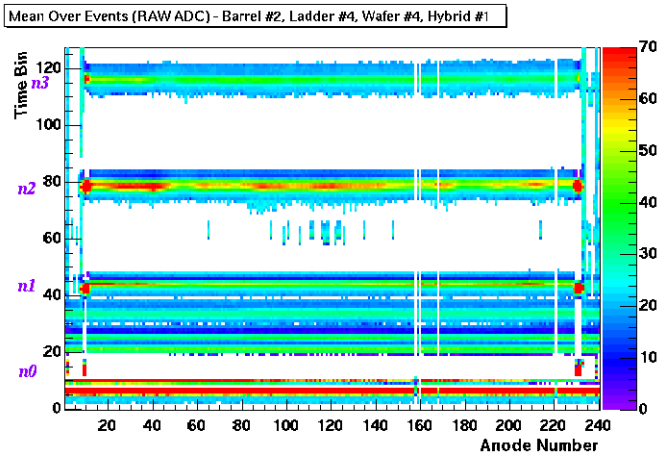

Figure 6.3: This picture shows the lines from the injectors. Three lines are clearly visible, only the first "n0" injector is not.

5 V, since with this pulse the injectors work the best even though it creates additional noise in the detector. In the year 2001 there were other problems concerning the detector. The main problem was a high noise in the detector. Because of this noise was the detector turned off for some time in order not to slow down the whole experiment by the big amount of data generated by the noise. This noise did not only complicated the reading of the particle hits, but also blurred the injector signals. In the Figure 6.4 are shown two injector events with the noise. In the beginning of year 2002 most of the noise was diagnosed to origin from bad grounding of the high-voltage power supply. After that was almost all noise in the detector, in physics events, removed,but there is still some noise remaining in the injector events at lower time bins.

As can be seen from the pictures, the drift speed calibration, using the injectors, is not just problematic, but there is a question if it can be done at all.

6.4 Injector functionality status

Since the injectors work only on same places, and suffer from the noise, we first of all have to know if there are some places where the injectors work properly all the time or at least most of the time. One of the things we need,

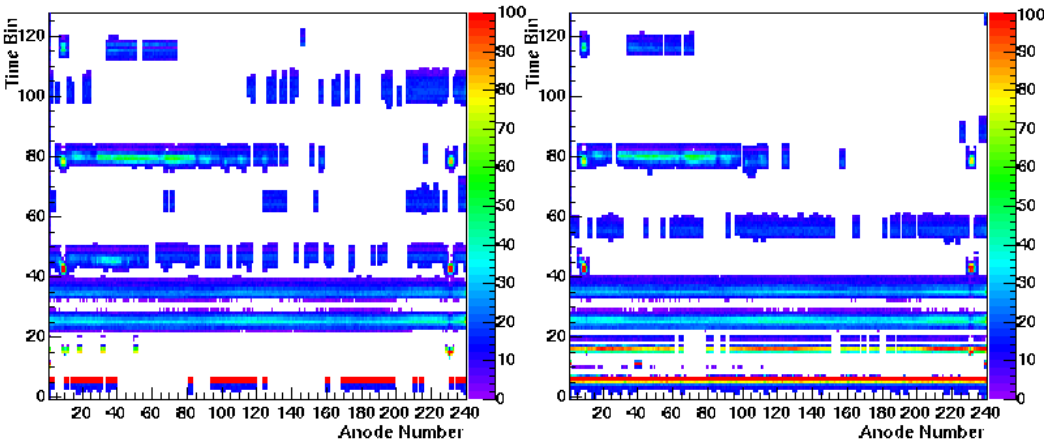

Figure 6.4: Two consecutive injector events with a varying noise.

is to separate the noise from the signal of the real injectors. Because the position of the noise varies with time, it is desirable to suppress the noise by averaging over a number of injector events. In these averaged events the signal from the noise, that shifts from place to place, will be lower, but the signal on places where the injectors work regularly every event will be the same, thus the signal to noise ratio will be increased. Another important question is whether the performance of the injectors changes with time as the detector is being used.

In the Figures 6.5, 6.6, and 6.7 are three pictures of the detectors on the same ladder of the middle barrel of SVT. These figures were made by averaging over 100 injector events. Data for each of the pictures were taken at different times. The data for the first Figure 6.5 of the averaged injector events were taken in July 2001 in the beginning of the 2001-year run. At that time the whole detector suffered from high noise, as shown in the Figure 6.4. It can be seen that, as we averaged over the 100 events, the noise was suppressed and the places, where the injectors worked regularly, stepped out. This also shows that the places, where the injectors work, do not change from event to event. If the behavior of the injectors was this constant over a long time, it would then be possible to choose the best visible lines and use them for calibration. To see the behavior of the injectors over a longer period of time there are the other two picture. The data for the Figure 6.6 were taken in the beginning of year 2002 shortly after most of the noise was removed, which shows as almost no background. Data for the last Figure 6.7

were taken in March 2002 before the STAR detector was disassembled, when the SVT was off for a longer period before the data were taken.

From this, and also other data taken during year 2001 and beginning of the year 2002, we can see some important issues concerning the functionality of the injectors of SVT. Even though the places, where the injectors work, don't change from event to event, they vary a lot on a longer term basis. So far it seems that the longer is the detector turned on, the better the injectors work, and also on more places. This means that the injectors work the worst shortly after the detector is turned on after a longer period when it was not used. Another issue is the prevailing noise in the beginning of the drift region. This noise is on all detectors and completely blurs the signal from the first injector "n0" which is around time bin 10. For this reason there are only three injectors that can be used for the calibration.

For the calibration we need to choose the best working parts of the injectors. If we look closely at the previous figures, there are only couple places where the injectors work every time. All these places are between anodes 9 and 11 or between anodes 230 to 232. These places are at the ends of injector lines. The injector lines end at the so called bonding pads, where is their size increased from 8 μm to about 100 μm in order to connect them with the voltage supply. These bigger parts of the injectors create greater signal and are thus more reliable. Because the spots from the bonding pads appear regularly in most events, we will use them for the calibration.

6.5 Drift speed calibrations using the injector bonding pads

As we have shown above, the injectors on SVT don't work properly. The injector events, instead of looking like in Figure 6.3, are usually like the event in Figure 6.4. We can see, that only the signal from the bonding pads is well visible. Because there can be a difference in the drift velocity inside one SDD we will separately analyze the spots at the first and last anodes. The size of the hits from the bonding pads are about three anodes wide. However some of the bonding pads do not work properly too, and some of the anodes on which lay the the bonding pads are damaged. For this reason the first thing to do was to map the detector and create a list of the good bonding pads that will be preferably used.

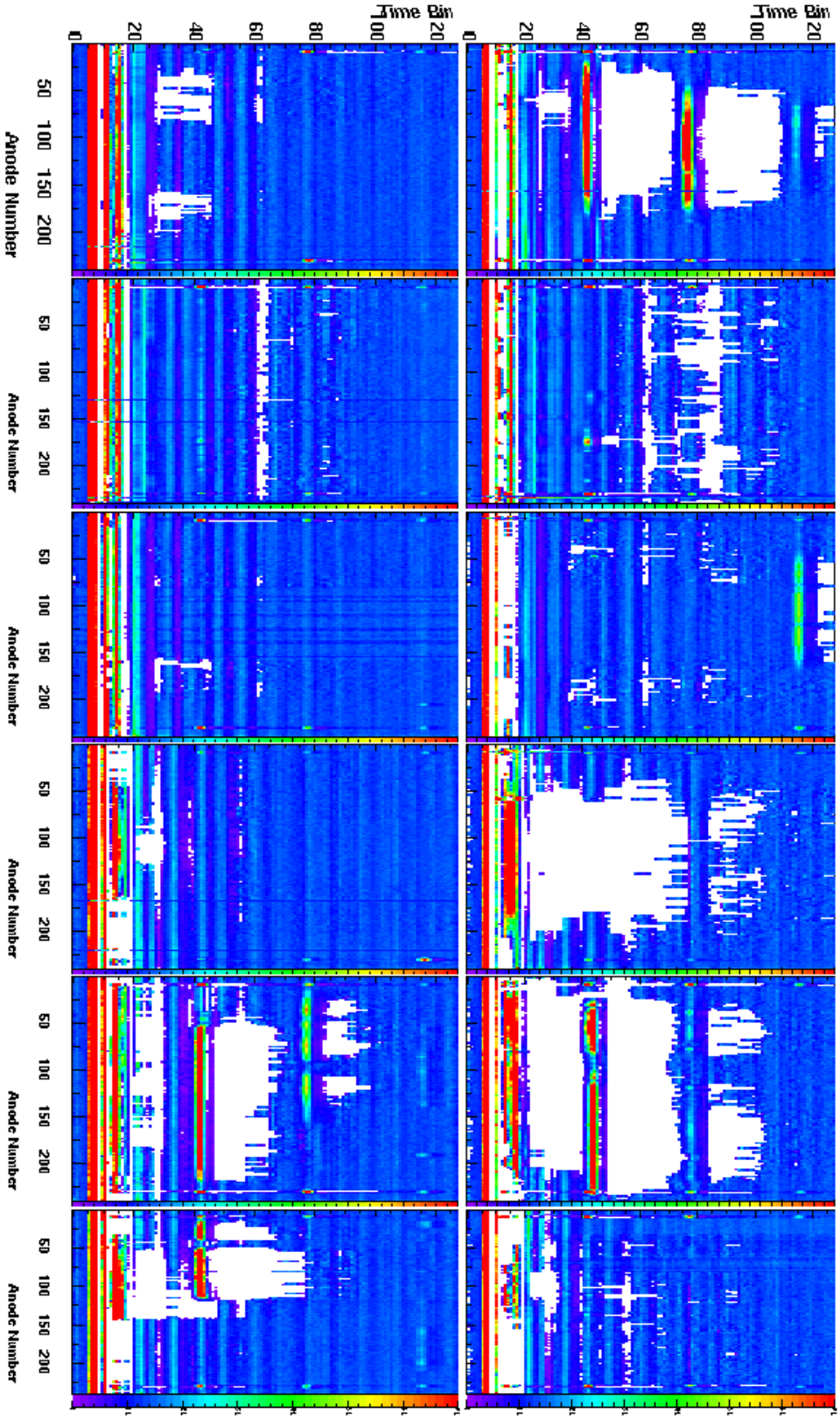

Figure 6.5:

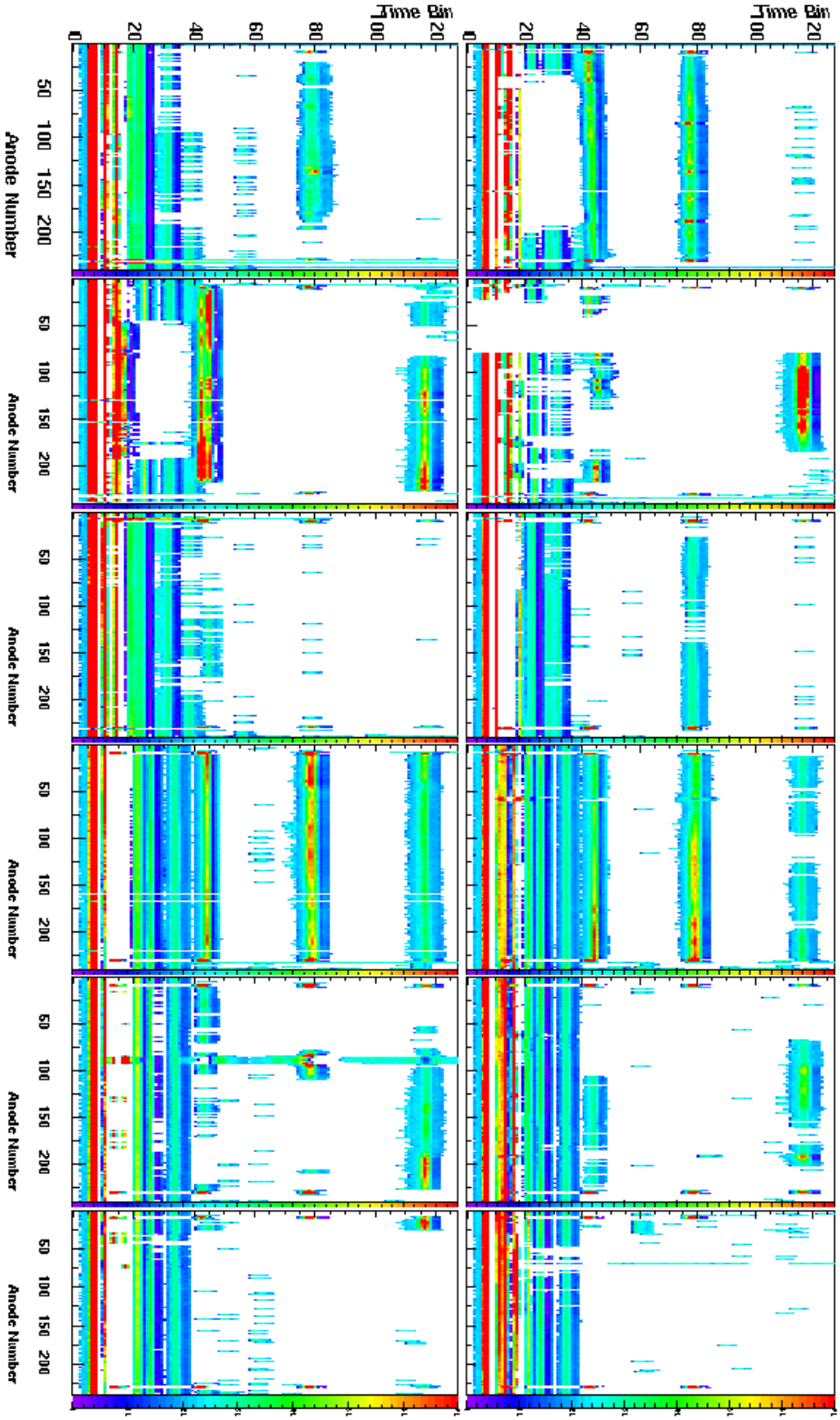

Figure 6.6:

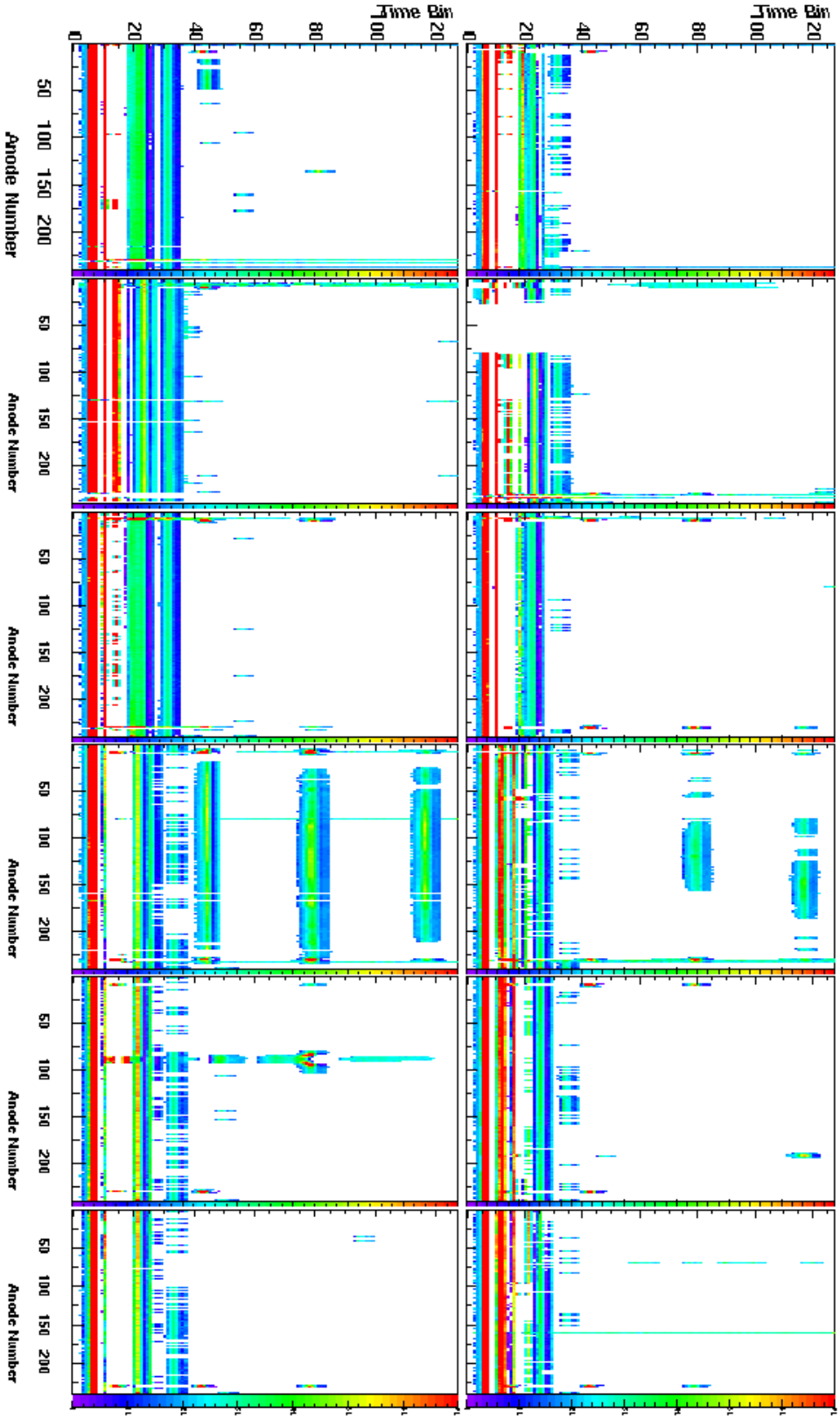

Figure 6.7:

We are interested in the time-position of the spots from the injectors. We will get the position by charge weighted average. In order to do this, we need to know the right value of the signal measured at the collecting anodes.

6.5.1 Signal mapping

When, in the SDD, the charge is registered at the collecting anodes, the signal is processed, and written to a 10-bit number. This signal in 10-bits is transmitted to the Data Acquisition (DAQ). The DAQ then sends all the data from all the sub-detectors to the storage. Because the speed of the data taking of the whole experiment is limited by the bandwidth between the DAQ and data storage, the data from SVT have to be sent in only 8-bit number. This means that all numbers in $\langle 0, 1023\rangle$ have to be mapped into $\langle 0, 255\rangle$. The mapping used in SVT is linear with two different slopes in two regions. The First interval $\langle 0, 127\rangle$ is mapped one-to-one into the same interval. The second interval $\langle 128, 507\rangle$ is mapped three-to-one into the interval $\langle 127, 254\rangle$. The rest of the interval $\langle 507, 1023\rangle$ is mapped into a single number 255.

During the analysis, the reverse mapping has to be done. Because all the bins above 507 are showing as 255, all the hits that saturate to 255 have to be discarded, since we cannot calculate their exact position.

6.5.2 Spectrum of individual hits

As an illustrative example we will take one of the detectors from the middle barrel. The injector event on one half-detector is shown in the Figure 6.8. We chose this detector, because it has good hits on all upper three injectors. The first "n0" injector is unrecognizable because of the noise. Since this is very common, we will not use the first injector for the calibration. This SDD represents quite well the rest of the SVT. In the following analyses we will show the results for the hits marked in the Figure 6.8. As stated before, the hits from the bonding pads are usually about three anodes wide. We get the time position of the injector hit by averaging over the hits on individual anodes belonging to the hit. Before that, we show in Figure 6.9 spectrum of hits on individual anodes for all three marked injector spots. The spectrum was made from 100 consecutive events. These events were taken within couple seconds so there is neglectable change in the temperature. They thus give a good estimate of the accuracy of the signal from the bonding pads.

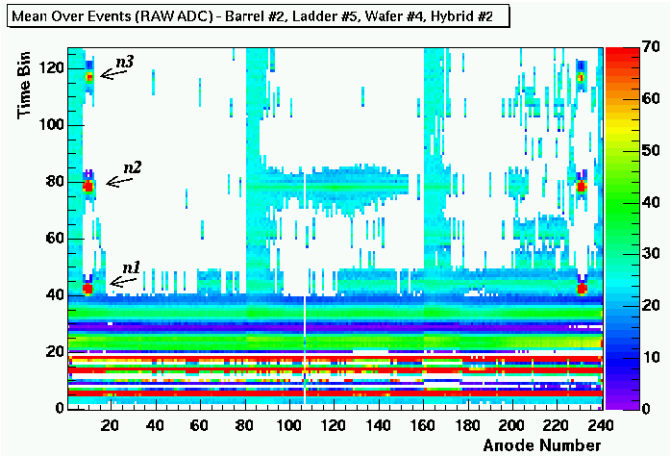

Figure 6.8: Injector event with visible hits from the injector bonding pads that can be used for the drift speed calibration.

From the Figure 6.9 we can see that the signal is about one time bin[2] wide and it's structure resembles three peaks. These three peaks are a result of the so called "t_0 jitter". We can greatly improve the accuracy by implementing a "t_0 jitter" correction.

T_0 jitter

The t_0 jitter comes from the timing of SVT and RHIC. At RHIC there are 57 bunches of gold ions traveling in the ring. The bunches cross at the interaction points on 105 ns intervals, which is known as the RHIC strobe or clock. SVT derives its timing from this RHIC strobe.

The measured signal of SVT is recorded by Switched Capacitor Arrays (SCA) (more about SVT's front-end electronics can be found in [24]). The SCAs are running at 8/3 of the RHIC strobe. This makes a SVT time bucket 40 ns long.

Because the SCAs are running at 8/3 RHIC strobe, there are 3 possible phases relative to the RHIC strobe at which the SCA's can be stopped, as shown in the Figure 6.10. The SCAs are stopped at the first possible full SCA clock after notification of the event. This phase is written out for each of the 24 individual Read Out (RDO) boards. Since we know which SDD belongs

[2] One time bin corresponds to about 300 μm distance in the drift direction.

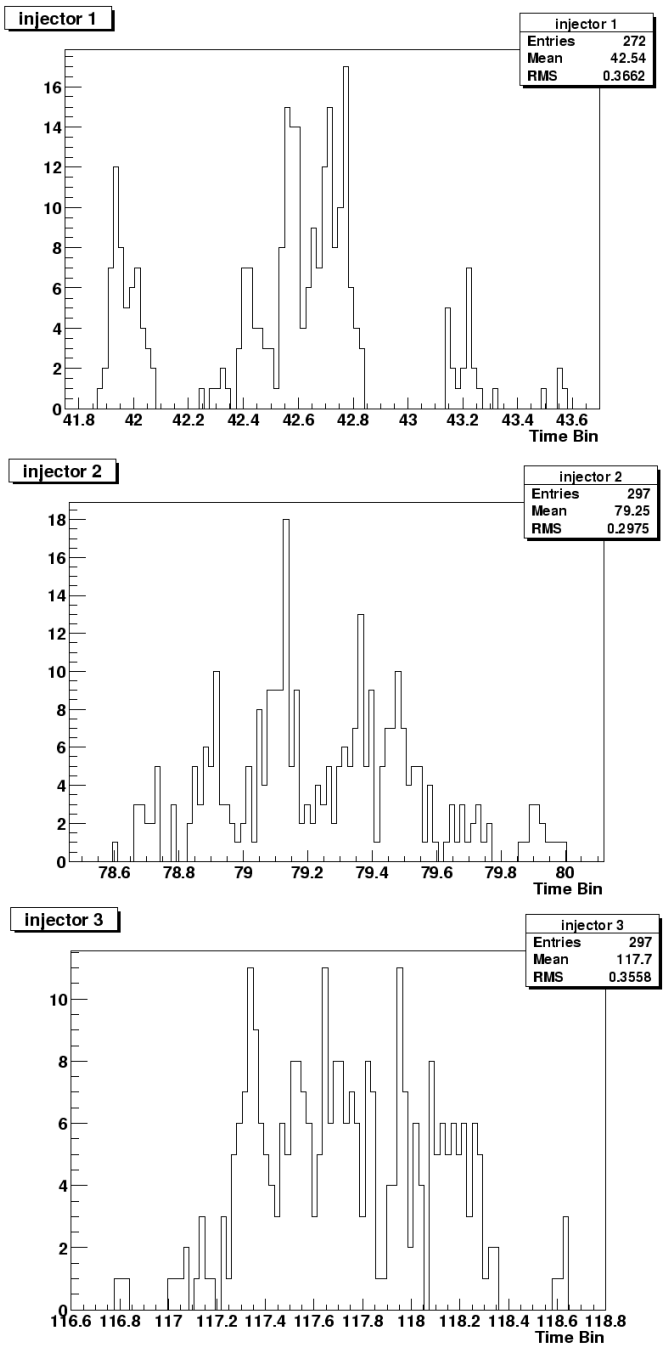

Figure 6.9: Spectrum of the time-positions of the hits on individual anodes for each injector.

to which RDO board, we know which phase to subtract. Looking at the Figure 6.10 we can have 3 offsets: $\Delta T_a = 0\ ns$, $\Delta T_b = 15\ ns$ and $\Delta T_c = 30\ ns$.

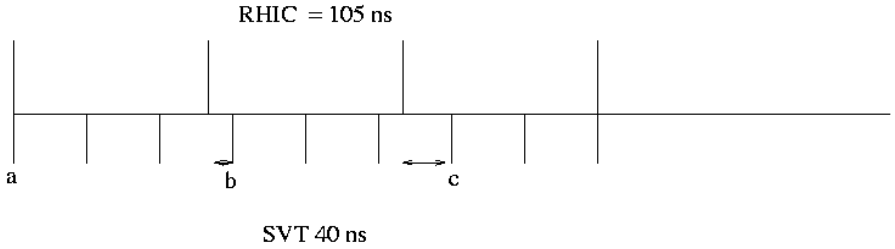

Figure 6.10: Schematic view of the difference between the RHIC and SVT timing.

6.5.3 Corrected injector signal

After performing the subtraction of the offset due to the "t_0 jitter" we obtain spectrum of the hits with smaller RMS, as shown in the Figure 6.11. Since the signal from the bonding pads is usually about three anodes wide, we can average over these anodes to get more precise position of the injector. The positions of the whole bonding pads are shown in the Figure 6.12. The resulting error in the drift time resolution is about ± 0.1, which corresponds to the error of about $30\mu m$ in the position resolution of the hit.

6.5.4 Temperature variations

All the previous computations were made to show the achievable accuracy of the calibration, if we use the signal from the injector bonding pads, instead of using the injector lines. However, as it was said earlier, there are temperature changes and fluctuations that influence the overall precision. There are two main types of temperature changes in the detector.

The first one is a periodic change with a period of about 2.5 minutes. It is caused by the temperature regulator of the SVT which tries to keep the detector's temperature constant. This fluctuation is always present and is about 1 K big.

The second temperature change occurs as the detector is turned on. The whole detector is water cooled and it takes some time till the whole detector is brought to the thermal equilibrium, and the temperature stabilizes. From the 2001 year run, it is estimated, that it takes about two hours. This temperature change is much bigger than the temperature fluctuations due to the temperature regulator.

To see the temperature changes, and estimate the accuracy of the calibration we were taking injector events for a period of 10 minutes with an injector event every 5 seconds. The data for the same injector as in the previous section are shown in the Figure 6.13. These figures show well the fluctuation with the 2.5 minute period for the upper two injectors. Signal for the first injector is little blurred by noise. We can see that, in an agreement with 6.4, the fluctuation grows with the drift distance.

In the previous figures were only the short-time fluctuations. The long-time fluctuations can be seen in the Figure 6.14. This figure was made using laser hits, which work quite well, but the lasers are mounted only on three places of the detector, and cannot thus track relative temperature changes in the different parts of the detector. This measurement was done shortly after the detector was turned on, and there is a well visible change in the average temperature. Note also that the position is split into three separate lines. This is because the "t_0 jitter" correction has not been applied.
In an ideal situation we could track both the long, and short-time temperature fluctuations. The quality of calibration depends on the sampling frequency of the injector events. To get our previous results we used 5 seconds long intervals. In normal physics run this is not possible, because this would slow down the experiment too much. In the physics run of year 2001 the injector triggers were fired every 200 seconds, which is not enough to track the short time fluctuations. What we then get, is the long-time temperature changes with bigger error that grows with the drift distance. At the maximum drift distance we get the error of about $\pm 10\ ns$, which corresponds approximately to $\pm 80\ \mu m$.

6.5.5 Number of working injectors

In the previous section we saw, that the calibration, using the signal from the injector bonding pads, is possible, when the signal is sufficient. Very important information is then a number of detectors that have working injectors. In the Figure 6.15 is shown the number of working injector bonding

pads that can be used for the calibration. On the x-axis are indexes of the individual half-detectors. The inner barrel has indexes from 0 to 63, the middle barrel is from 64 to 207, the remaining indexes are from the outer barrel. As can be seen from the Figure 6.15, the worst part of the whole detector is the innermost barrel. Out of the eight ladders, there are only two that have some working injectors that can be used for the calibration. This means that the rest of the inner barrel will have to be calibrated using only some approximation based on those two calibrated ladders. The injectors of the middle and outer barrel are working better. About two thirds of the detectors have one or more bonding pads producing a good signal.

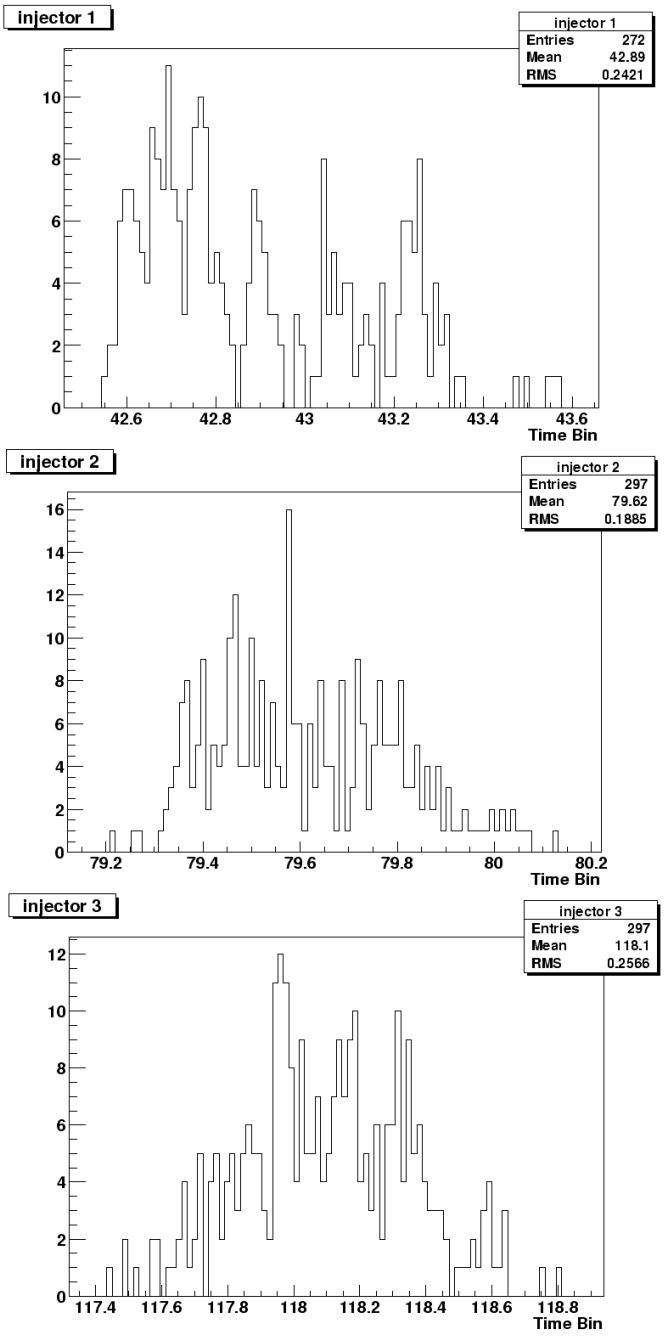

Figure 6.11: Spectrum of the time-positions of the hits on individual anodes for each injector after performing the "t_0 jitter" correction.

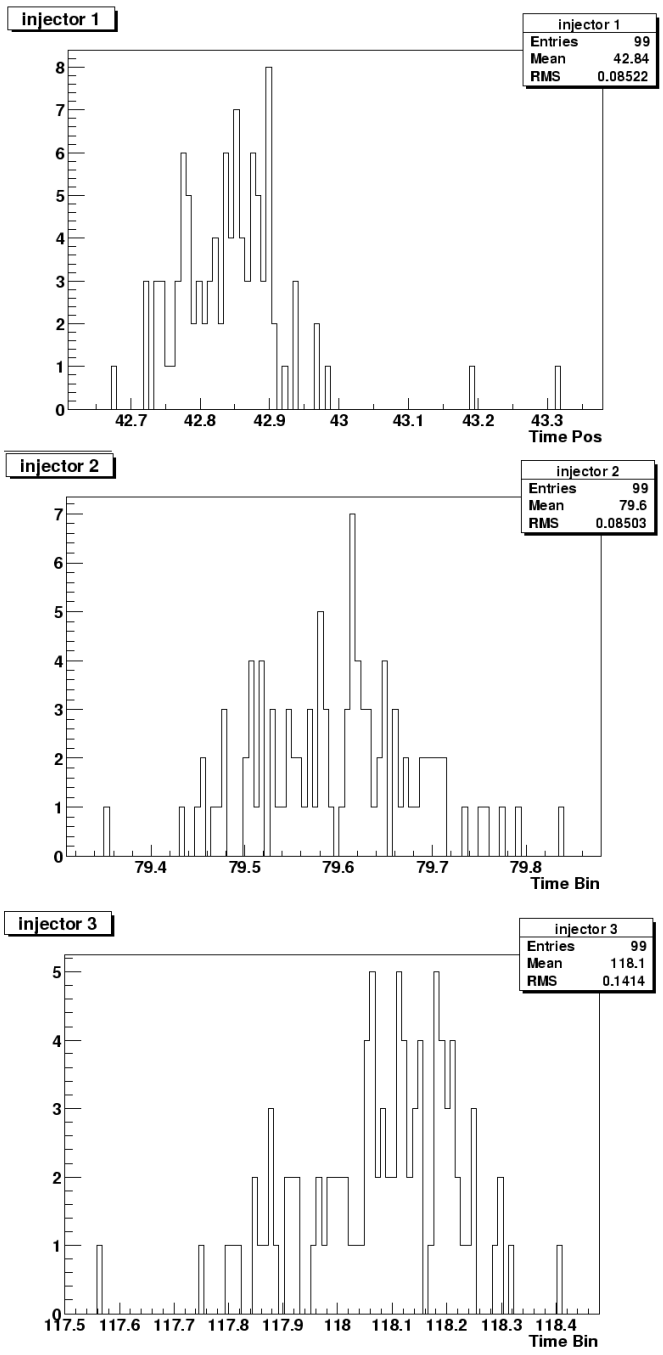

Figure 6.12: Time-position of the whole bonding pad hits from the three selected injector pads.

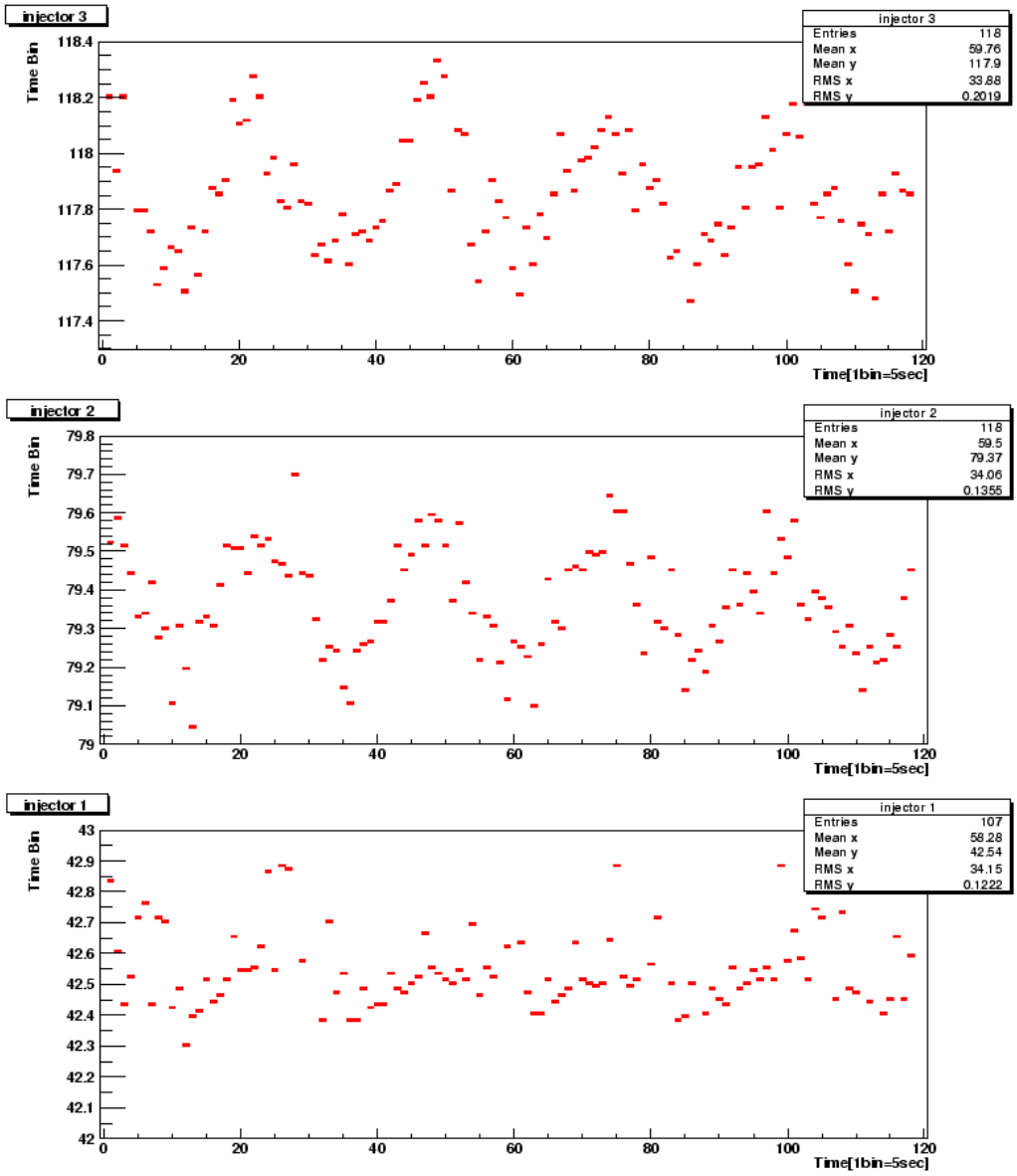

Figure 6.13: Hits from injector bonding pads showing the changes in their time-position over 10 minutes. Individual hits are 5 seconds apart.

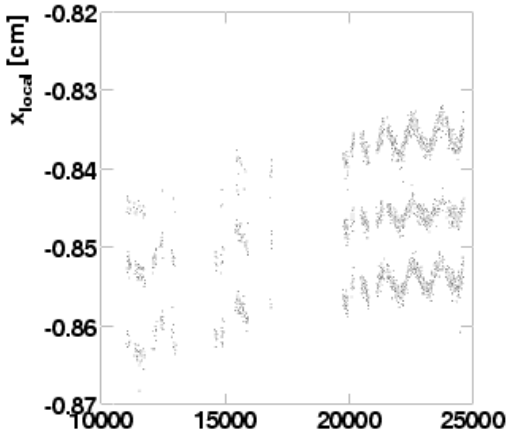

Figure 6.14: Long-time drift speed fluctuations due to the temperature variation measured by a laser. The position of the laser is showed in the detectors local coordinates, where one time bin corresponds to about 0.03 *cm*. On the x axis is a number of the event; the whole range corresponds to about 30 minutes long run. Figure was obtained from STAR/SVT Collaboration.

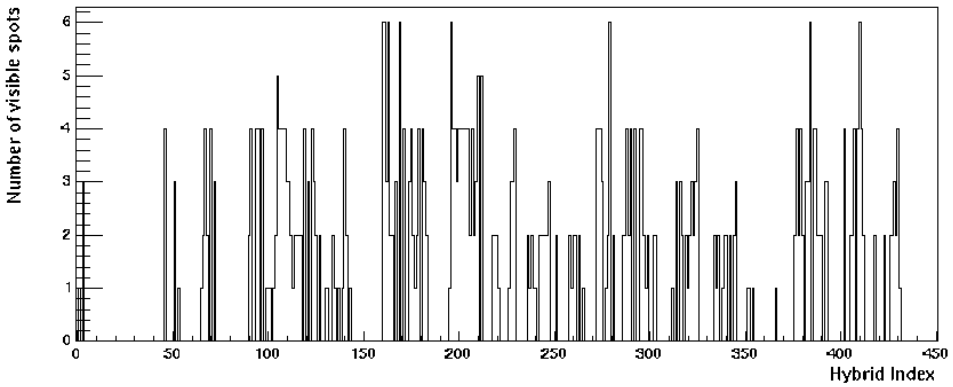

Figure 6.15: Number of good injector pads that can be used for calibration. We are using upper three injectors, so the maximum number of possibly used pads is six.

Chapter 7

Event-by-Event Analyses

As the heavy-ion experiments reach higher and higher energies and multiplicities, going from AGS to SPS, and finally to RHIC, the statistical means of study become more accessible and important, not only for multi-event characteristic, but also in single event spectra. Our task is to distinguish dynamical and statistical fluctuation, since the first ones carry important physics information about the collision. The higher are the multiplicities, the more precise study can be done inside single events, and details on smaller scales revealed. In event-by-event analyses we determine the degree of correlation of the multiparticle final state for individual events of a large event ensemble.

The study of correlations and fluctuations is important in probing the dynamic history of the collision. In our study we will use the apparatus of normalized factorial moments to study the correlation strength dependency on the pseudorapidity.

7.1 Basic formalism

In the following analyses we will use the formalism of *multiparticle correlators* and *factorial moments* as described in [6].

Let's consider a nucleus-nucleus collision which produces a number of n particles into the whole phase space Ω_{tot}. The distribution of the particles in a sub-volume Ω is fully described by the exclusive distribution $P_n(y_1, \ldots, y_n)$, where y describes the position of the particle in the phase space. However, in real experiment, we cannot measure the *exclusive* distribution. We thus have to consider the corresponding *inclusive* distribution $\rho_n(y_1, \ldots, y_n)$. The

relation between the exclusive and inclusive distributions is:

$$\rho_n(y_1,\ldots,y_n) = P_n(y_1,\ldots,y_n) + \sum_{m=1}^{\infty} \frac{1}{m!} \int_\Omega P_{n+m}(y_1,\ldots,y_n,y_1',\ldots,y_m') \prod_{i=1}^{m} dy_i'. \tag{7.1}$$

The inclusive densities ρ_n are normalized as:

$$\begin{aligned} \int_\Omega \rho_1(y)dy &= \langle n \rangle, \\ \int_\Omega \rho_2(y_1,y_2)dy_1dy_2 &= \langle n(n-1) \rangle, \\ \int_\Omega dy_1 \ldots \int_\Omega dy_q \rho_q(y_1,\ldots,y_q) &= \langle n(n-1)\ldots(n-q+1) \rangle. \\ &\ldots \end{aligned}$$

The inclusive q-particle distributions $\rho_q(y_1,\ldots,y_q)$ contain contributions from the lower-order distributions. For our study is useful to use a defined sequence of functions $C_q(y_1,\ldots,y_q)$ that have the property of vanishing whenever any two of their arguments become statistically independent. These quantities are the *correlation functions*, sometimes also called the *cumulant functions*. The inclusive densities can then be expanded in the terms of the cumulant functions:

$$\rho_1(y) = C_1(y), \tag{7.2}$$

$$\rho_2(y_1,y_2) = C_1(y_1) + C_1(y_2) + C_2(y_1,y_2), \tag{7.3}$$

$$\begin{aligned} \rho_3(y_1,y_2,y_3) &= C_1(y_1)C_1(y_2)C_1(y_3) + C_1(y_1)C_2(y_2,y_3) \\ &\quad + C_1(y_2)C_2(y_1,y_3) + C_1(y_3)C_2(y_1,y_2) + C_3(y_1,y_2,y_3). \end{aligned} \tag{7.4}$$

This expansion can be generalized for all orders of the inclusive distributions.

7.1.1 Factorial moments

Let's now consider the probability P_n for producing a total population of n particles:

$$P_n = \frac{\sigma_n^{excl}}{\sigma_{inel}}. \tag{7.5}$$

The generating function for the P_n distribution is defined as:

$$G(w) = \sum_{n=0}^{\infty} P_n w^n. \tag{7.6}$$

The q-order partial derivative of 7.6 with respect to w at $w = 1$:

$$\tilde{F}_q = \frac{\partial^q}{\partial w^q} G(w)\Big|_{w=1} \tag{7.7}$$

$$= \sum_n P_n \; n(n-1)\ldots(n-q+1) \tag{7.8}$$

$$= \int_\Omega dy_1 \ldots \int_\Omega dy_q \rho_q(y_1, \ldots, y_q) \tag{7.9}$$

is called the q-order *factorial (or binomial) moment.* The 7.6 can then be rewritten using 7.7:

$$G(w) = 1 + \sum_{q=1}^{\infty} \frac{(w-1)^q}{q!} \tilde{F}_q. \tag{7.10}$$

Using the decomposition 7.4 of the inclusive densities, we can manipulate 7.6 to:

$$\ln G(w) = \sum_{q=1}^{\infty} \frac{(w-1)^q}{q!} f_q, \tag{7.11}$$

where the f_q are the *unnormalized factorial cumulants*:

$$f_q = \int_\Omega dy_1 \ldots \int_\Omega dy_q \; C_q(y_1, \ldots, y_q). \tag{7.12}$$

For manual computations it is helpful to rewrite P_n and f_q in the form similar to 7.7:

$$f_q = \frac{\partial^q}{\partial w^q} \ln G(w)\Big|_{w=1}, \tag{7.13}$$

$$P_n = \frac{1}{n!} \frac{\partial^n}{\partial w^n} G(w)\Big|_{w=0}. \tag{7.14}$$

It is important to note the relationship between the factorial moments $\tilde{F}_q$ and the factorial cumulants f_q. We get the relationship by comparing the right-hand terms of 7.10 and 7.11:

$$\exp\{\sum_{q=1}^{\infty} \frac{(w-1)^q}{q!} f_q\} = 1 + \sum_{q=1}^{\infty} \frac{(w-1)^q}{q!} \tilde{F}_q. \tag{7.15}$$

By expanding the exponential and comparing coefficients of the same power of $(w-1)$ we get:

$$\begin{aligned}
\tilde{F}_1 &= f_1, \\
\tilde{F}_2 &= f_2 + f_1^2, \\
\tilde{F}_3 &= f_3 + 3f_2f_1 + f_1^3, \\
\tilde{F}_4 &= f_4 + 4f_3f_1 + 3f_2^2 + 6f_2f_1^2 + f_1^4, \\
\tilde{F}_5 &= f_5 + 5f_4f_1 + 10f_2f_3 + 10f_3f_1^2 + 15f_2^2f_1 + 10f_2f_1^3 + f_1^5.
\end{aligned}$$

In general

$$\tilde{F}_q = q! \sum_{\{l_i\}_q} \prod_{j=1}^{q} \left(\frac{f_j}{j!}\right)^{l_j} \frac{1}{l_j!}, \tag{7.16}$$

where $\{l_i\}_m$ are all the sets of non-negative integers that satisfy the condition

$$\sum_{i=1}^{m} i l_i = m. \tag{7.17}$$

From the equation 7.12 we can see from that, whenever there are no multi-particle correlation in the system, all the factorial cumulants of $q > 1$ are zero. In such a case the factorial moments reduce to

$$\tilde{F}_q = (f_1)^q = \langle n \rangle^q . \tag{7.18}$$

For this reason it is convenient to introduce the *normalized factorial moments* of the q-order F_q as

$$F_q = \frac{\tilde{F}_q}{(f_1)^q} = \frac{\langle n(n-1)\ldots(n-q+1)\rangle}{\langle n \rangle^q}, \tag{7.19}$$

which approache 1 as the correlation between q-tuples in the system, on the scale given by the subsystem Ω, gets weaker.

As an example of the use of the tools defined above, we can study two statistical distributions with different properties. The first distribution is the *Poisson distribution*

$$P_n = e^{-\langle n \rangle} \frac{\langle n \rangle^n}{n!}. \tag{7.20}$$

This distribution can principally be derived by considering independent, equally probable fluctuations. This property should show in the factorial

moments and cumulants. To obtain explicitly the factorial moments we first use 7.6 to get the generating function

$$G(w)_{Poisson} = \sum_{n=0}^{\infty} P_n w^n = \exp\{\langle n\rangle (w-1)\}. \tag{7.21}$$

From 7.7 we then get the factorial moment of any order as:

$$\tilde{F}_q = \frac{\partial^q}{\partial w^q} G(w)_{Poisson}\Big|_{w=1} = \langle n\rangle^q . \tag{7.22}$$

From 7.19 then follows that normalized factorial moments of all orders are 1, which is in an agreement with the Poisson distribution as description of many independent, equally probable fluctuations.

Second example is the *geometrical distribution*

$$P_n = (1-\alpha)\alpha^n; \quad \alpha = \frac{\langle n\rangle}{1+\langle n\rangle}, \tag{7.23}$$

which compared to the Poisson distribution is very wide. The generating function is then

$$G(w)_{geom} = \sum_{n=0}^{\infty} P_n w^n = \frac{1-\alpha}{1-\alpha w}. \tag{7.24}$$

The factorial moments from 7.7 are

$$\tilde{F}_q = \frac{\partial^q}{\partial w^q} G(w)_{geom}\Big|_{w=1} = q!\frac{\alpha^q}{(1-\alpha)^q}. \tag{7.25}$$

Since

$$\langle n\rangle = \frac{\alpha}{1-\alpha}, \tag{7.26}$$

the normalized factorial moments for the geometric distributions are

$$F_q = \frac{\tilde{F}_q}{\langle n\rangle^q} = q!. \tag{7.27}$$

The normalized factorial moments, as defined by 7.19, posses very important property of a Poisson fluctuation suppression, as shown in [34]. If the multiplicity distribution contains correlations, the fluctuations due to these correlations will remain in the normalized factorial moments. However the fluctuating due to finiteness of the bins or single particle detector acceptance cancels out in the normalized factorial moments. This is a very important property that, for example, doesn't hold for normalized moments $\langle n^q\rangle / \langle n\rangle^q$.

7.2 Analyses description

In this work we will concentrate on the study of two-particle correlations in the multiplicity distribution using the normalized factorial moments of second order (F_2). We will be searching for the correlations in pseudorapidity windows η as a function of the size of these windows.

For our analyses we have a set of *minimum bias* data with about 140 000 events. The structure of these data is dominated by the geometry of the collisions, which means that most of the data comes from the peripheral collisions.

For the coming analyses it is important to know, how is the centrality of the events computed. The Glauber model, described in [12] [33], gives the relationship between the collision geometry and the final multiplicity. This model can calculate an average charged hadron multiplicity as a function of the impact parameter. In the STAR we use the charged hadron multiplicity of the event to get the centrality. All the events are divided into a number of centrality bins, depending on the total multiplicity. However the measured centrality can be, due to the fluctuations of the particle production, created in events with different centralities, as shown in the Figure 7.1, taken from [33]. This figure shows the particle multiplicities distribution measured at

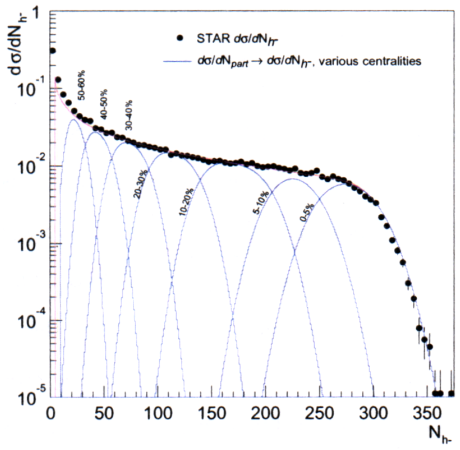

Figure 7.1: Fit to the multiplicity distribution of negatively charged hadrons using the Glauber model.

STAR with the shown fit from the Glauber model. From the figure we can

also see that, as we go from high to small centralities, the fluctuation in the impact parameters increases inside of each centrality bin. These fluctuations can influence the analyses.

As previously stated, we study correlations in the pseudorapidity windows in the mid-rapidity region. We will study the normalized factorial moment F_2 in a pseudorapidity window $|\eta| < \eta_{max}$ as a function of the size of this window η_{max}.

7.3 Used data cuts

In order to study the physically interesting dynamical fluctuations we need to introduce additional cuts on data in order to suppress fluctuations from inefficiencies and other experimental effects.

vertex position

There are necessary cuts for the vertex position along the beam axis. The first one comes from the detector's finite acceptance in pseudorapidity. The maximum window in pseudorapidity η, we will study, is from -1 to 1. We need to select only those events that will be fully covered by the detector in this pseudorapidity window. In such a case the standard cut used at the STAR collaboration[35] is to choose only the events with a vertex z-position between ± 75 cm from the center of the detector. This way the analyses will not be influenced by the fluctuations in the position of the vertex.

The central membrane, which brings the high voltage to the TPC and divides it into two semi-volumes, can cause some problems in the analyses. At first the electric field close to the membrane is not mapped very accurately. For this reason some tracks may seem split and be accounted as two different tracks. More important is, however, the multiple scattering of particles in the membrane itself. This effect is most important for low momentum particles traversing the membrane. These particle can undergo multiple rescattering in the membrane, and thus blur the correlation signal. For this reason we will cut out events that lie in the middle of the detector under the central membrane, because they produce the highest number of particles traveling along the membrane. We choose this area to be between ± 10 cm. This way any particle with $\eta < 0.05$ cannot cross the central membrane.

track splitting

Track splitting happens when, during the computer reconstruction, a track from one real hit is reconstructed as two different tracks. Tracks like this then lie close to each other and create false signal that shows as higher correlation in small pseudorapidity windows. To prevent this phenomena, we use an information about the number of hits found in the TPC for each track.

As the tracks are reconstructed, the reconstruction program calculates, and writes down the number of possible maximum hits that could have been found in TPC for the track that was reconstructed if it left the best possible ionization signal. If a track is split into two, we want to choose just one of them. For this reason we demand, that all tracks we use, must have a ratio of the number of hits actually found in the TPC to the number of hits that could have been found greater then 0,52. This is a standard cut used in the STAR collaboration [35].

transversal momentum

We can obtain interesting informations by looking at different parts of the transversal momentum spectra, since they can reflect different parts of the collision and different physical processes leading to its production. At this point, however, we also need to know about the detection and reconstruction efficiency.

In the Figure 7.2, taken from [33], we can see a single particle reconstruction efficiency for π^-. We see that the efficiency for particles with $p_\perp < 100\ MeV/c$ is close to zero. For this reason, we will use only tracks with $p_\perp > 100\ MeV/c$. As we can see the efficiency changes rapidly in the region of $100 - 400\ MeV/c$ and then it flattens. The single particle efficiency should cancel out of the normalized factorial moments. However, if there is also an efficiency depending on the correlated part of the two particle density (C_2), the normalized factorial will not cancel it out, and it will show in the analyses. We may suppose that the efficiencies are connected . For this reason we will study separately the region with $p_\perp < 400\ MeV/c$ and $p_\perp > 400\ MeV/c$.

pion identification

Because we want to see effects connected with boson, like the Bose-Einstein's effect, we need cuts that will enhance the relative amount of identical bosons(

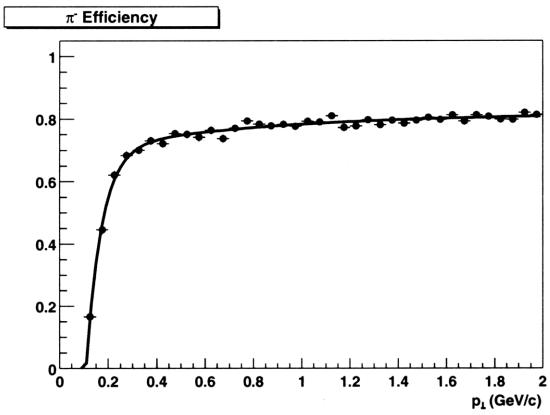

Figure 7.2: The track reconstruction efficiency for π^- as a function of $p_\perp$. Figure from [33].

in our case pions) in our data sample.

STAR uses the ionization information $\frac{dE}{dx}$ from TPC and, in future, also from SVT. In the Figure 7.3 we show the plot of $\frac{dE}{dx}$ versus momentum for our min. bias data. We clearly see the different branches belonging to different particle species, that are described by the Bethe-Bloch formula. The pions are best separable from other particle species below the momenta of $600 MeV/c$. In our analyses we will use two cuts in oder to enhance the pion population in our sample. The First cut we will use is based on a variable z defined in [33] as

$$z = \ln\left(\frac{I_m}{I_h}\right), \tag{7.28}$$

where I_m is the measured ionization of a given track, and the I_h is the theoretical ionization from Bethe-Bloch formula for the given particle species. This variable has a Gaussian distribution around zero for the given particle species. In our analyses we chose a $p_\perp$ cut described in the Table 7.3. This cut is based on the data published in [33]. More about this variable and particle identification by $\frac{dE}{dx}$ can be found in [33].

If we want to get a cleaner data sample we have to make restriction in the momentum, because for higher momenta the branches of different particle species merge, and the identification via $\frac{dE}{dx}$ is not possible anymore. The cleanest sample we will use, will be restricted in the transversal momenta by

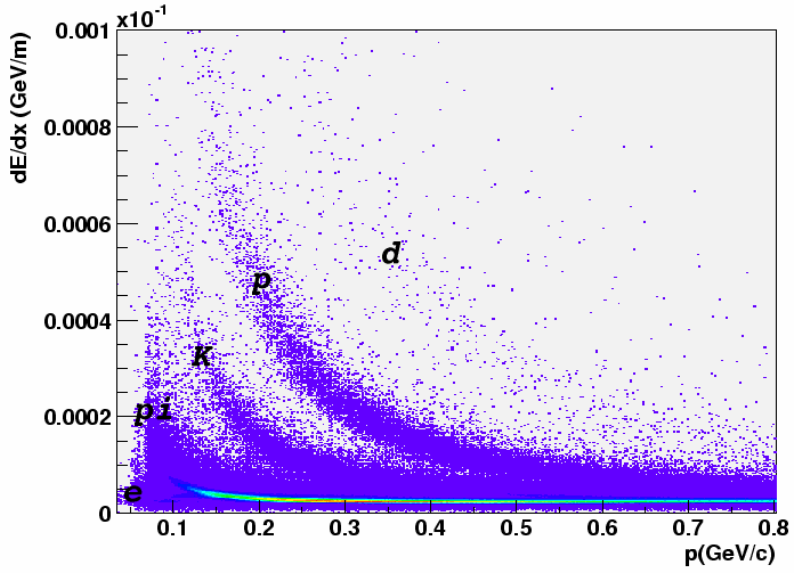

Figure 7.3: Particle identification by $\frac{dE}{dx}$ plot versus the total momenta p as measured by TPC. The different branches correspond to different particle species.

the cut $p_\perp < 600\ MeV/c$.

Together with the cut, that was done because of the detector efficiency, our mostly used sample will be in the $p_\perp$ range: $400\ MeV/c < p_\perp < 600\ MeV/c$.

7.4 Analyses Results

As a first thing, we will study the dependence of the normalized factorial moments F_2 for negative pions on the centrality of the collision. In the Figure 7.4 are plotted the F_2 normalized moments as a function of η_{max} for the four most peripheral centrality bins. In the Figure 7.5 are the same plots for the four most central collisions. For these plots we used the data that have about 30 000 events with 40 000 charged tracks in the peripheral collisions, and about 4 000 most central events with about 400 000 charged tracks.

There are interesting facts that can be observed from these plots. As we

$p_\perp$ range[GeV/c]	z cut
$0.40 < p_\perp < 0.45$	$z < 1$
$0.45 < p_\perp < 0.50$	$z < 0$
$0.45 < p_\perp < 0.55$	$z < -1$
$0.55 < p_\perp < 0.60$	$z < 1$

Table 7.1: Cuts for different values of $p_\perp$ used for identification of pions from the measured $\frac{dE}{dx}$ information.

go from the highest centrality bins to the most peripheral ones, the average value of F_2 increases. This can be explained in the terms of fluctuation of the impact parameter. As it was stated in the previous chapter and showed in the Figure 7.1, the most peripheral centrality bins contain the highest fluctuations. For this reason the next plots, we will study, will be from the most central collisions.

The graphs in Figure 7.5 also show that, for small pseudorapidity windows, the correlation increases, and there is a significant peak around zero. This agrees with the predictions of the HBT interferometry. Note also, that, as we go to the most central events, the correlation increases as well. We can see that the correlation also slowly increases for the largest windows. This can be partially described by the fluctuation in the impact parameter. However, we are mainly interested in the area of small pseudorapidity windows, where the Bose-Einstein effect is visible, which clearly is a multiboson effect.

We can now look at the area of small η_{max} in a detail. This will of course be at the cost of larger statistical errors. In the Figure 7.6 is shown the F_2 in quarter the window as in the previous figures. In this figure are shown separately data for positive, and negative pions, and also for all the pions together. All the shown data are only for the most central events at the energies of $0.4\ GeV < p_\perp < 0.6\ GeV$.

We can see that, for small windows, there is a correlation that drops almost to 1 at about $\eta_{max} = 0.2$ for all three data sets. For $\eta_{max} > 0.2$ the multiplicity can be considered to almost obey the Poisson distribution.

Before making any conclusions, we should show the influence of the cuts, we chose in the previous section. In the Figure 7.7 are shown the normalized factorial moments in the most central centrality bin for three different $p_\perp$ cuts. We can see that all three curves radically differ in the small pseudorapidity windows. The cut we reasoned in the previous section and used so

far for all the data ($0.4\ GeV < p_\perp < 0.6\ GeV$) shows well the Bose-Einstein effect. But the other two cuts are completely different.

The F_2 with the cut choosing the lowest $p_\perp$ particles seems to raise, where the peak from Bose-Einstein effect starts. This cut takes particles from the part of $p_\perp$ spectrum, where the single-track reconstruction efficiency is very low. Even though, we do not know what is the two-track reconstruction efficiency, we suppose that a dropping efficiency in the two-track reconstruction causes this effect.

We also see that F_2, for the high $p_\perp$ part of the multiplicity distribution, falls rapidly when reaching $\eta_{max} = 0.2$. In this part of the $p_\perp$ spectrum plays very important role the effect of track merging. The track merging happens when two close tracks from two particles are reconstructed as one. This effect grows with $p_\perp$, since the tracks for particles with high $p_\perp$ have almost straight tracks. Such particles do not separate enough on their way trough the TPC.

Another effect that takes place in the area of small η_{max} is the Coulombic repulsion of particles of the same charge that are close to each other.

Both these effects are important in the HBT interferometry and we should know about them. The Figure 7.7 shows that our analyses is very sensitive to the cuts we make. For accurate results it is necessary to make good corrections.

7.4.1 Theoretical check

In the shown figures we can see the Bose-Einstein effect, which is usually measured by the HBT interferometry. However what we see, compared to the HBT[37], is a very faint signal. The peak for the most central collision, where it is best visible, is only about 0.01 high from the base. For comparison, in HBT this rise is more then 0.2.

We have to expect our correlation to be weaker, since the correlation due to the Bose-Einstein effect is strongest for particles that are close to each other in the momentum space. When we are looking for the correlation in pseudorapidity, we are actually making an integration over the azimuthal angle, so we are also including particles that can be far from each other in the momentum space. We can, however, check with a theory, if our analyses roughly agrees.

A theoretical prediction for the correlations in the rapidity windows were made by Andreev in [36]. At our energies the rapidity and pseudorapidity

are almost equal, so we can use the prediction for the pseudorapidity as well. We get the F_2 as

$$F_2(\Delta\eta) = 1 + \int_{\eta_1}^{\eta_2} d\eta_1 \int_{\eta_1}^{\eta_2} d\eta_2 \; C_2(\eta_1, \eta_2) / \left(\int_{\eta_1}^{\eta_2} \; \rho_1(\eta) d\eta \right)^2 . \tag{7.29}$$

In [36] is shown that this integration leads to:

$$F_2(\Delta\eta) \approx 1 + \frac{\pi\delta^2}{2\sqrt{1 + \alpha^2 \cosh{(\eta_1 + \eta_2)/2}}} \Psi(\frac{\Delta\eta}{2\delta}), \tag{7.30}$$

where

$$\Psi(x) = \frac{2}{x^2} \left[x \; \mathrm{arctg} x - \frac{1}{2} \ln{(1 + x^2)} \right] . \tag{7.31}$$

The important variables are $\alpha^2 \approx \tau^2/R^2$ and $\delta^2 \approx 1/\left\langle k_T^2 \right\rangle R^2$, where τ/R is a ratio of a duration of the emitting source to its size (as measured by HBT), and k_T is the transverse momentum. We have $\langle k_T^2 \rangle \approx (500 \; MeV)^2$, and from [37] we can take α to be about 1.

Since we are interested in the narrowest mid-rapidity bin we used ($\eta_{1,2} = \pm 0.0125$), we have $(\eta_1 + \eta_2) = 0$, and $\Delta\eta = 0.025$. Now we can simplify 7.30 to

$$F_2(\Delta\eta) \approx 1 + \frac{\pi\delta^2}{2\sqrt{2}} \Psi(\frac{\Delta\eta}{2\delta}). \tag{7.32}$$

From [37] we get $R \approx 6 \; fm$. The δ^2 is then about $\delta^2 \approx 1/230$, and $\frac{\Delta\eta}{2\delta} \approx 0.18$. The 7.31 is then approximately 1, which gives very simple 7.32 as

$$F_2(\Delta\eta) - 1 \approx \frac{\pi\delta^2}{2\sqrt{2}} \approx 0.005. \tag{7.33}$$

Even though this is a very crude approximation, and our analyses suffers from high statistical errors, the result of 7.33 quite agrees with our correlation analyses.

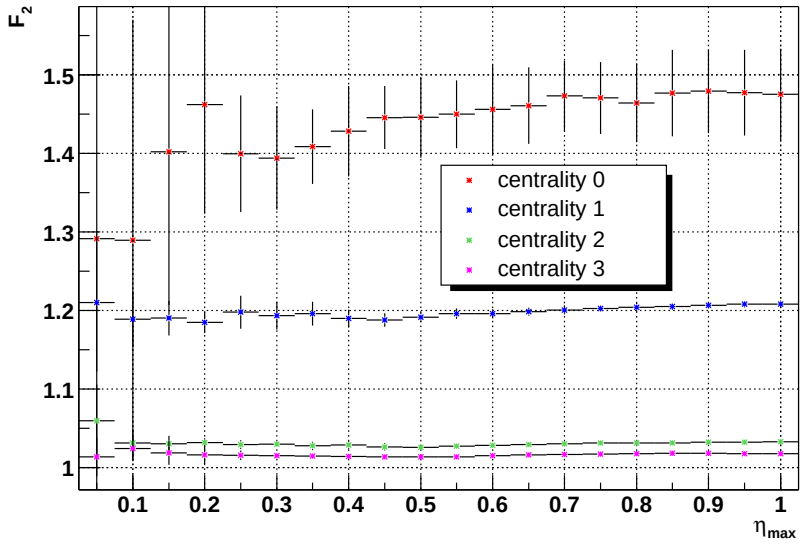

Figure 7.4: Dependence of the F_2 on η_{max} for different centrality bins in peripheral collisions.

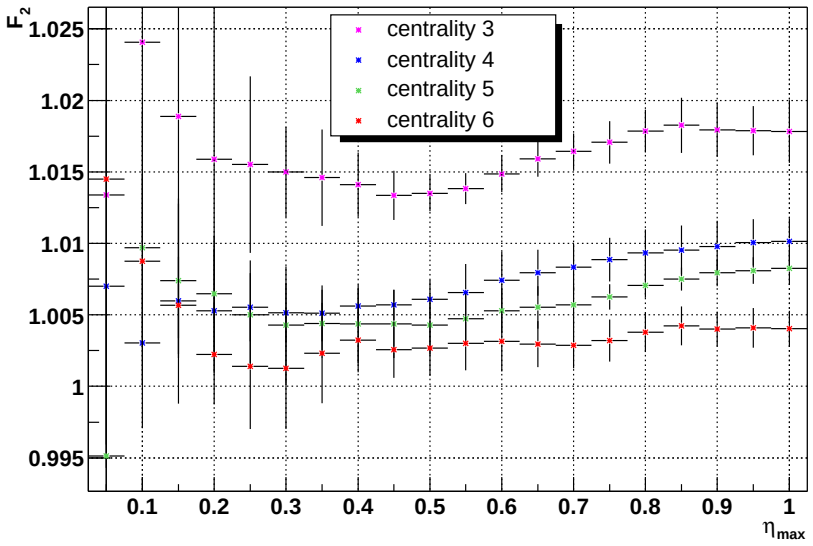

Figure 7.5: Dependence of the F_2 on η_{max} for different centrality bins in the most central collisions.

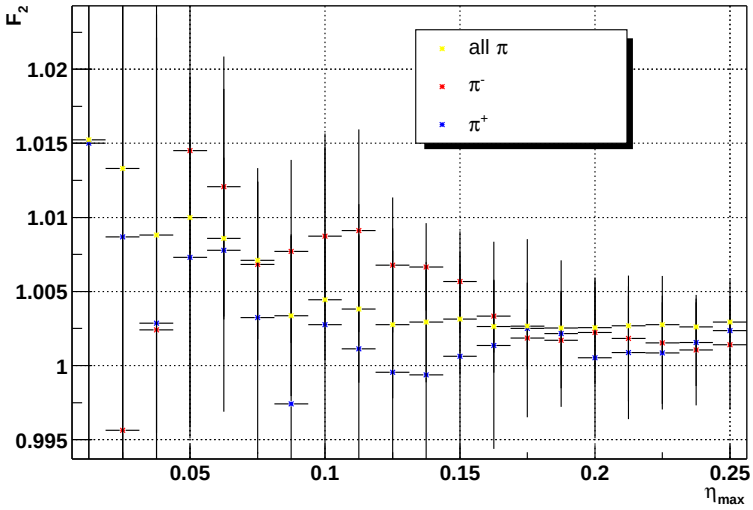

Figure 7.6: Detail of the F_2 in the most central collisions for $0.4\ GeV < p_\perp < 0.6\ GeV$.

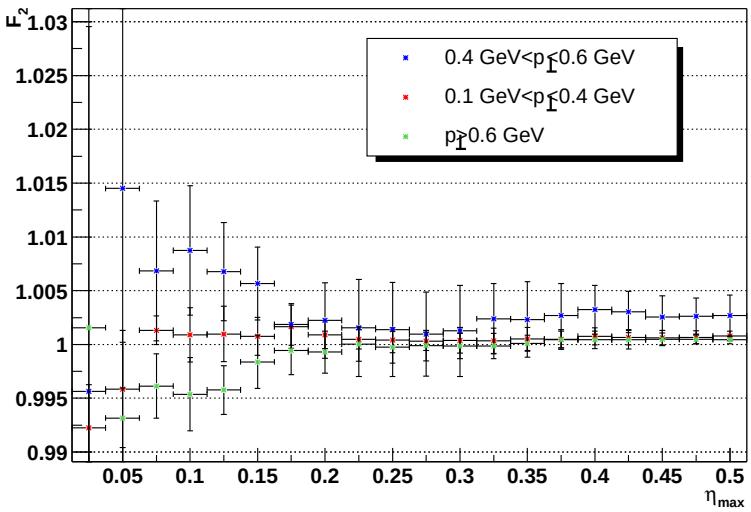

Figure 7.7: Dependence of F_2 on different $p_\perp$ cuts. The data are from the most central collisions.

Chapter 8

Conclusion

8.1 Conclusion on SVT drift speed calibration

We have showed the possibility to use the MOS injectors for the drift speed calibration and estimated the resolution. This was the first time that the "t_0 jitter" correction was applied. It is also a first estimate of the resolution that could be achieved in the next year's run, because in the year 2000 and 2001 runs were performed no temperature dependent drift speed calibrations.

The injectors are working very irregularly. The only places, where is their signal visible most of the time, are very small areas of the bonding pads. Even thought the signal from these bonding pads is usually only three anodes wide, it is possible to use it for the calibration. The accuracy of the calibration is mainly influenced by the temperature fluctuation due to the thermal regulation of the water cooling system. We cannot calibrate for this short-time fluctuations, because the injector sampling frequency is not high enough.

There are, however, some possibilities to improve the accuracy that should be considered. If we suppose that the phase of the fluctuations is the same for the whole detector, we could use a laser injectors to measure the phase continuously and then approximate the fluctuations for the rest of the detector. Another possibility is to take the injector measurements more frequently for only couple of SDDs, and approximate the rest. This procedure should improve the accuracy mainly for the longer drift times.

8.2 Conclusion on the data analyses

We have used the technique of normalized factorial moments to study two-particle correlations in the multiplicity distribution. Based on literature, we have chosen different cuts in order to choose suitable data for the analyses. Even though this analyses was very simple in principle, and was done only in the pseudorapidity, we could see the Bose-Einstein effect, and checked that what we see, agrees with the theory. We were also able to see the differences between the different centralities, and showed that they have to be studied separately.

This analyses showed the importance of the corrections for different effects, like the track merging or Coulombic repulsion, if we want to achieve better precision. The correction for track merging can be done by making mixed pairs from different events the same way as it is done in the HBT analyses. The same technique of normalized factorial moments can be used for more then two-particle correlations, but it needs the corrections and better statistics that will be available in the coming years of the experiment.

Bibliography

[1] G.Baym: *From dreams to beams in two decades*, Proc. of QM2001, Nucl. Phys. **A698** (2002) xxiii-xxxii.

[2] T. Roser: *RHIC performance*, Proc. of QM2001, Nucl. Phys. **A698** (2002) 23c-28c.

[3] For overview of RHIC experiments see: *Proc. of QM2001*, Nucl. Phys. **A698** (2002) 29c-77c;

[4] C.A. Ogilvie: *Review of Nucler Reactions at the AGS*, Proc. of QM2001, Nucl. Phys. **A698** (2002) 3c-12c.

[5] C. Lourenço: *Searching for Quark Matter at the CERN SPS*, Proc. of QM2001, Nucl. Phys. **A698** (2002) 13c-22c.

[6] E.A. De Wolf, I.M. Dremin, W. Kittel: *Scaling laws for multiparticle dynamics and fluctuations in multiparticle dynamics*, Phys. Rep. **270** (1996)1.

[7] J.Chýla: *Quarks, partons and Quantum Chromodynamics*, Prague Theory Papers 1997: *http//:www-hep.fzu.cz/Theory/notes/p1997.html* (1997).

[8] R.D.Field: *Aplications of Perturbative QCD*, Addison-Wesley (1989).

[9] J.D.Bjorken, S.D.Drell: *Relativistic Quantum mechanics* and Relativistic Quantum fields, McGraw-Hill (1965).

[10] K. Moriyasu: *An Elementary Primer for Gauge Theory*, World Scientific Pub. Co. (1983).

[11] M.Creutz: *Quarks, Qluons and Lattices*, Cambride University Press (1983).

[12] C.Wong: *Introduction to High-Energy Heavy-Ion Collisions*, World Scientific Publishing Co. Pte. Ltd. (1994).

[13] J.M. Rubio: *Transverse Flow from m_T Spectra in Pb+Pb Collisions at 158 GeV/c per Nucleon*, University of Geneva, master thesis No 2974 (1998)

[14] A.Chodos et al.: *New extended model of hadrons*, Phys.Rev. **D9**, 3471-3495 (1974).

[15] L.D.Landau and E.M.Lifshitz: *Statistical Physics*, Pergamon Press, Oxford (1980).

[16] T.Matsui and H.Satz, *Phys. Lett. B178, 416 (1986)*; T.Matsui: Zeit. Phys. **C38**, 245 (1988).

[17] C. Gale: *Direct photons and thermal dilepton: A theoretical review*, Proc. of QM2001, Nucl. Phys. **A698** (2002) 143c-152c.

[18] H. Caines: *Strangeness production at RHIC ,Proc. of QM2001*, Nucl. Phys. **A698** (2002) 112c-117c.

[19] V.B. Berestetskii, E.M. Lifshitz, and L.I. Pitaevskii: *Quantum Electrodynamics*,Pergamon Press, Oxford, 1982.

[20] H. Naef: *Particle correlations in fixed targed Pb+Pb collisions at 158 GeV/c per nucleon*, University of Geneva, master thesis No 2947 (1997)

[21] F. Retièr et al.: *The STAR Time Projection Chamber,Proc. of QM2001*, Nucl. Phys. **A698** (2002) 408c-411c.

[22] J.W. Harris and the STAR Collaboration: *The STAR Experiment at the Relativistic Heavy Ion Collider*, Nucl. Phys **A566** (1994) 277c.

[23] J. Takagashi *et al.*: *Silicon drift detectors for STAR/SVT experiment at RHIC*, Nucl. Inst. and Meth. **A439** (2000) 497-506.

[24] D. Lynn *et al.*: *The STAR silicon vertex tracker: a large area silicon drift detector*, Nucl. Inst. and Meth. **A447** (2000) 264-273.

[25] R. Bellwied *et al.*: *Electron Injection in Semiconductor Drift Detectors*,Elsevier Preprint (1998).

[26] J. Blaizot: *The Quark-Gluon Plasma and Nuclear Collisions at High Energy*, Elsevier Science (1998).

[27] U.A.Wiedemann, U.Heinz: *Particle Interferometry for relativistic Heavy-Ion Collisions*, Phys. Rep. **319** (1999) 145-230.

[28] E.Gatti,P.Rehak(1984): *Semiconductor Drift Chamber - an application of a novel charge transport scheme*, Nucl. Instr. and Meth. **225** (1984), 608.

[29] D.M. Read: *The Silicon drift detectors and its use in a Vertex Tracker*, dissertation, The University of Texas at Austin (1996)

[30] G.Lutz: *Semiconductor Radiation Detectors*, Springer-Verlag (1999)

[31] D.J.Gross and F.Wilczek: *Phys. Rev. Lett.* **30** (1973) 1343.

[32] R. Hanbury Brown, R.Q. Twiss: *Phil. Mag.* **45** (1954) 633.

[33] M.C. de la Barca Sánchez: *Charged Hadron Spectra in Au+Au collision at* $\sqrt{S_{NN}} = 130\ GeV$, dissertation, Yale University (2001).

[34] P. Carruthers: *Fractal Structures and Correlations in Hadronic Multiparticle Distributions*, Int. Jour. of Modern Phys. **A4** 20(1989) 5587-5614.

[35] STAR Collaboration:*Phys. Rev. Lett* **87**, 8(2001)

[36] I.V Andreev:*Phys. Atom. Nucl* **58** (1995)495

[37] F.Laue for STAR Collaboration: *Two Particle Interferometry at RHIC*, Proc. of QM2001, Nucl. Phys. **A698** (2002) 177c-184c.